NAVAL POSTGRADUATE SCHOOL

MONTEREY, CALIFORNIA

THESIS

MOLTEN SAND INDUCED DEGRADATION OF ULTRA HIGH TEMPERATURE CERAMIC DIBORIDES

by

Collin L. Vorbroker

June 2023

Thesis Advisor: Troy Ansell
Second Reader: Young W. Kwon

THIS PAGE INTENTIONALLY LEFT BLANK

REPORT DOCUMENTATION PAGE	*Form Approved OMB No. 0704-0188*

1. AGENCY USE ONLY *(Leave blank)*	**2. REPORT DATE** June 2023	**3. REPORT TYPE AND DATES COVERED** Master's thesis

4. TITLE AND SUBTITLE
MOLTEN SAND INDUCED DEGRADATION OF ULTRA HIGH TEMPERATURE CERAMIC DIBORIDES

5. FUNDING NUMBERS

6. AUTHOR(S) Collin L. Vorbroker

7. PERFORMING ORGANIZATION NAME(S) AND ADDRESS(ES)
Naval Postgraduate School
Monterey, CA 93943-5000

8. PERFORMING ORGANIZATION REPORT NUMBER

9. SPONSORING / MONITORING AGENCY NAME(S) AND ADDRESS(ES)
N/A

10. SPONSORING / MONITORING AGENCY REPORT NUMBER

11. SUPPLEMENTARY NOTES The views expressed in this thesis are those of the author and do not reflect the official policy or position of the Department of Defense or the U.S. Government.

12a. DISTRIBUTION / AVAILABILITY STATEMENT
Approved for public release. Distribution is unlimited.

12b. DISTRIBUTION CODE
A

13. ABSTRACT (maximum 200 words)

The desire for increased performance of gas turbine engines (GTE) is leading to higher operational temperatures within GTEs. Thermal and environmental barrier coatings (T/EBC) applied to turbine blades (typically the hottest component) allow for temperatures to reach as high as 1700 °C. T/EBCs; however, they are susceptible to deterioration when in contact with liquified atmospheric particulates. These particulates are composed of varying amounts of calcia, magnesia, alumina, and silicates (CMAS). At elevated GTE operating temperatures, the molten CMAS attacks the T/EBC, greatly reducing the performance and lifespan of turbine blades. The goal of this thesis is to examine how three different ceramic compositions withstand CMAS penetration. The ceramics are hafnium diboride (HfB2), zirconium diboride (ZrB2), and a high entropy ceramic diboride (Ta0.20, Zr0.20, Nb0.20, Hf0.20, Ti0.20)B2. The ceramics were exposed to a 1:1 CMAS water slurry then placed in the furnace at 1300°C and 1600°C for 1 and 10 hours. The samples were then analyzed via scanning electron microscope (SEM) and x-ray diffraction (XRD) to identify CMAS penetration and reaction products. Nano-indentation hardness testing was then performed to evaluate how the CMAS impacted the hardness. All samples experienced CMAS intrusion and oxidation with varying effects on the material's nano-hardness.

14. SUBJECT TERMS
UHTC, hafnium diboride, HfB2, zirconium diboride, ZrB2, high entropy ceramics, (Ta0.20, Zr0.20, Nb0.20, Hf0.20, Ti0.20)B2, sand intrusion, sand phobic, CMAS

15. NUMBER OF PAGES
103

16. PRICE CODE

17. SECURITY CLASSIFICATION OF REPORT	**18. SECURITY CLASSIFICATION OF THIS PAGE**	**19. SECURITY CLASSIFICATION OF ABSTRACT**	**20. LIMITATION OF ABSTRACT**
Unclassified	Unclassified	Unclassified	UU

NSN 7540-01-280-5500

Standard Form 298 (Rev. 2-89)
Prescribed by ANSI Std. 239-18

THIS PAGE INTENTIONALLY LEFT BLANK

Approved for public release. Distribution is unlimited.

MOLTEN SAND INDUCED DEGRADATION OF ULTRA HIGH TEMPERATURE CERAMIC DIBORIDES

Collin L. Vorbroker
Lieutenant, United States Navy
BSE, Miami University, 2015

Submitted in partial fulfillment of the
requirements for the degree of

MASTER OF SCIENCE IN MECHANICAL ENGINEERING

from the

NAVAL POSTGRADUATE SCHOOL
June 2023

Approved by: Troy Ansell
Advisor

Young W. Kwon
Second Reader

Brian S. Bingham
Chair, Department of Mechanical and Aerospace Engineering

THIS PAGE INTENTIONALLY LEFT BLANK

ABSTRACT

The desire for increased performance of gas turbine engines (GTE) is leading to higher operational temperatures within GTEs. Thermal and environmental barrier coatings (T/EBC) applied to turbine blades (typically the hottest component) allow for temperatures to reach as high as 1700 °C. T/EBCs, however, are susceptible to deterioration when in contact with liquified atmospheric particulates. These particulates are composed of varying amounts of calcia, magnesia, alumina, and silicates (CMAS). At elevated GTE operating temperatures, the molten CMAS attacks the T/EBC, greatly reducing the performance and lifespan of turbine blades. The goal of this thesis is to examine how three different ceramic compositions withstand CMAS penetration. The ceramics are hafnium diboride (HfB2), zirconium diboride (ZrB2), and a high entropy ceramic diboride (Ta0.20, Zr0.20, Nb0.20, Hf0.20, Ti0.20)B2. The ceramics were exposed to a 1:1 CMAS water slurry then placed in the furnace at 1300°C and 1600°C for 1 and 10 hours. The samples were then analyzed via scanning electron microscope (SEM) and x-ray diffraction (XRD) to identify CMAS penetration and reaction products. Nano-indentation hardness testing was then performed to evaluate how the CMAS impacted the hardness. All samples experienced CMAS intrusion and oxidation with varying effects on the material's nano-hardness.

THIS PAGE INTENTIONALLY LEFT BLANK

TABLE OF CONTENTS

LIST OF FIGURES

LIST OF TABLES

THIS PAGE INTENTIONALLY LEFT BLANK

LIST OF ACRONYMS AND ABBREVIATIONS

AFRL	Air Force Research Lab
Al_2O_3	aluminum oxide, alumina
B	boron
B_2O_3	boric oxide
$(Ca\text{-}Mg)CO_3$	dolomite
$CaCO_3$	calcium carbonate
CaO	calcium oxide, calcia
$CaSO_4$	calcium sulfate
CMAS	calcia-magnesia-alumina-silicate
CMC	ceramic matrix composite
CO	carbon monoxide
CTE	coefficient of thermal expansion
EDS	energy dispersive X-ray
Fe_2O_3	iron oxide
GTE	gas turbine engine
HEB	high entropy boride
HfB_2	hafnium diboride
HfC	hafnium carbide
HfN	hafnium nitride
HfO_2	hafnia
MgO	magnesium oxide, magnesia
$MoSi_2$	molybdenum disilicide silicon nitride (Si_3N_4)
Nb	niobium
PDF	powder diffraction file
PM_{10}	particulate matter less than 10 μm in aerodynamic diameter
$PM_{2.5}$	particulate matter less than 2.5 μm in aerodynamic diameter
Pt	platinum

SEM	scanning electron microscope
Si_3N_4	silicon nitride
SiC	silicon carbide
SiO_2	silicon dioxide, silica
SPS	spark plasma sintering
T/EBC	thermal and environmental barrier coatings
Ta	tantalum
Ti	titanium
TSP	total suspended particle matter
UHTC	ultra-high temperature ceramics
WC	tungsten carbide
Wt.%	weight percent
XRD	X-ray diffraction
Y	yttrium
Y_2O_3	yttrium oxide, yttria
YSZ	yttria partially stabilized zirconia
ZrB_2	zirconium diboride
ZrO_2	zirconium dioxide, zirconia

ACKNOWLEDGMENTS

First, I want to thank Dr. Troy Ansell. Your guidance and expertise throughout this process were instrumental in honoring the memory and work of the late Dr. Andy Nieto. Between always being available to help me and the incalculable number of hours spent training/retraining me on the equipment, I truly could not have done it without you.

A very special thanks to my family, friends, and classmates for supporting and believing in me throughout my time at NPS. You made my time here enjoyable, and I will look back on it with fond memories, Thank you!

THIS PAGE INTENTIONALLY LEFT BLANK

I. INTRODUCTION

A. BACKGROUND AND MOTIVATION

Gas Turbine Engines (GTEs) are critical components of the United States military since they are used in everything from powering the M1 Abrams tank, to propelling and providing power to most USN ships, to aircraft and hypersonic vehicles. In addition to their military applications, they are used by all commercial airlines around the world. GTEs are engineering masterpieces made possible by the symbiosis of multiple engineering fields to include fluids and thermodynamics, structures and machine design, and material science. The more GTEs are used the more is demanded from them meaning researchers are constantly looking for ways to increase their performance.

Increased performance demands of GTEs led to increased efficiencies. One of the most common ways to increase the efficiency of a GTE is to increase the operating temperature [1]. The increase in operating temperatures has resulted in a need for new composite materials that can withstand these increased temperatures. In some cases the turbine inlet temperature exceeds 1400°C, with future targets of 1800°C [1]. These materials must not only be resilient to thermal degradation but must also be resilient to other environmental factors such as corrosion or environmental particulate attack. The main particulate that plagues engine performance is sand, which consists primarily of calcium oxide (or calcia, CaO), magnesium oxide (or magnesia, MgO), aluminum oxide (or alumina, Al_2O_3) and silicates (minerals based on silicon oxide, SiO_2), known together as CMAS.

The very high melting points of ceramic carbides, nitrides and borides make them potential candidates for use in these applications [2]. Carbides are classified as either ionic, covalent, or interstitial based on their primary bond type. Ionic carbides are extremely brittle and covalent carbides are very hard with great stability but are also brittle and difficult to produce. Ceramic nitrides are also hard to fabricate in pure form. Of the three classes, interstitial carbides are the best option with their extremely high melting temperatures, hardness and chemical and thermal stability [2]. Borides do not have as high

a bond strength or melting temperature as carbides but have a low coefficient of thermal expansion making them more shock and oxidation resistant [2].

The current technologies to handle these increased temperatures are single crystal superalloys coated with ceramic thermal and environmental barrier coatings (T/EBC). These have their limits and are not able to survive the higher target temperatures. One possible solution is the use of ceramic matrix composites (CMCs). CMCs have several advantageous qualities that make them good candidates for use in high temperature GTEs. Even though they are ceramic they can show fracture toughness like that of metals meaning they are more durable. These composites are also less dense than comparable aerospace metals and can handle significantly higher temperatures. Two drawbacks to CMCs, however, are microstructural changes induced at moderate temperatures and degradation of the fiber properties at elevated temperatures which results in reduced mechanical performance [1].

One of the most common T/EBC ceramic topcoats currently being used is yttria (Y_2O_3) partially stabilized zirconia (ZrO_2) or (YSZ) [3]. YSZ performs well as a thermal barrier coating but struggles when exposed to molten CMAS. The temperature at which CMAS begins melting at is around 1250°C extending to 1500°C, well below the target temperature of next generation GTEs [4]. Thus, some scientists and researchers are turning to rare earth phosphates to counter molten CMAS. Some of the potential candidate materials include zirconium boride (ZrB_2); hafnium boride (HfB_2); and Zr, Hf, titanium (Ti), niobium (Nb), and tantalum (Ta) combined with B in what is known as high entropy boride (HEB). Borides are being increasingly explored because they possess great thermal and electrical conductivities as well as low coefficients of thermal expansion, something that is critically important in low tolerance environments such as GTEs [5].

The next chapter summarizes what is currently known about CMAS attack on T/EBCs and HfB_2, ZrB_2, and HEB properties. These borides are being analyzed to better understand how they are affected by CMAS attack and their feasibility as UHTC coatings used in GTEs.

B. THESIS OBJECTIVES

The goal of this thesis research is to achieve a better understanding of the effects CMAS has on the properties of bulk samples of HEB, HfB_2, and ZrB_2. This will be achieved by analyzing the impact that temperature and exposure time have on the microstructure and composition of these borides. The hardness of these boride materials will be evaluated to determine how it varies within the affected zones of the material as well as between the different exposure conditions. The ultimate objective of this work is to determine which boride composition is most susceptible to CMAS attack and which composition could be a viable option for use in next generation GTEs.

THIS PAGE INTENTIONALLY LEFT BLANK

II. LITERATURE REVIEW

A. CMAS LITERATURE REVIEW

1. Sand Composition

During military operations in the Middle East, it was discovered that the projected service life of GTEs was being cut short mainly due to failure of components in the hot section of the engine. Failure analysis revealed that this was caused by deposit build up in the engine. It was determined that these deposits were a result of molten sand entering the engine and cooling on the blades [6], [7]. Thus, the interest in research of CMAS infiltration methods and resistance techniques gained substantial interest. To be able to counter CMAS infiltration, researchers needed to first determine what the CMAS is composed of.

Smialek et al. [6] were some of the first to look into airfoil degradation caused by sand ingestion. They noted that sand ingestion and compressor blade erosion resulted in significant power loss of the turbine. Samples primarily from eastern Saudi Arabia were analyzed and it was found that finer particles had more CaO, Al_2O_3, iron oxide (Fe_2O), and MgO while coarser sands from dried riverbeds were predominantly CaO and MgO with high carbon and sulfur content. XRD analysis showed that dune sand consisted primarily of crystalline quartz while riverbed sand was mainly calcite ($CaCO_3$) and dolomite ((Ca-Mg)CO_3) [6]. The breakdown of components by sand type is displayed in Table 1.

Table 1. Saudi Arabia sand composition. Source: [6].

	Dune Sand	20 µm Fines	10 µm Saudi No.1†	Riverbed Sand	100 µm Saudi No. 5†
SiO_2	90.8	52.4	55	12.3	28.7
CaO	1.5	17.4	20.9	25.9	11.6
Al_2O_3	2.5	14.3	13.6	5.2	4.1
Fe_2O_3	0.8	8.8	8.2	0.9	0.7
MgO	0.5	4.4	‡	15.6	54.9
NiO	1.0	0.5	NA	0.2	NA
TiO_2	0.2	0.9	2.2	0.2	NA
Na_2O	0.2	‡	NA	0.2	NA
K_2O	0.5	‡	trace	0.1	NA
CO_2	5.6	NA	NA	39.4	NA
SO_2	1.3	NA	NA	8.5	NA

Emission spectroscopy, normalized to 100% oxide.
NA - not analyzed
† From BFLRF No. 294.[4]
‡ Not found.

In a study performed by the Desert Research Institute, Engelbrecht et al. [8] evaluated 15 locations throughout the Middle East analyzing the composition of air suspended particulate matter. Total suspended matter (TSP), 10 µm aerodynamic diameter (PM_{10}), and 2.5 µm aerodynamic diameter ($PM_{2.5}$) filters were used to compare the particulate composition at each area. The samples consisted of a mixture of carbonates, oxides, salts, silicate minerals, and sulfates in varying quantities. Although the composition consisted of a variety of particles some are significantly more prevalent than the rest: SiO_2, Al_2O_3, CaO, and MgO [8]. Material compositions for each filter size are shown in Figure 1. They then compared the Middle East samples with dust samples collected from deserts around the world; the results are shown in Figure 2. This showed that the Middle East dust is consistent with dust from around the world but has higher concentrations of CaO and MgO and lower concentrations of Fe_2O_3 and MgO.

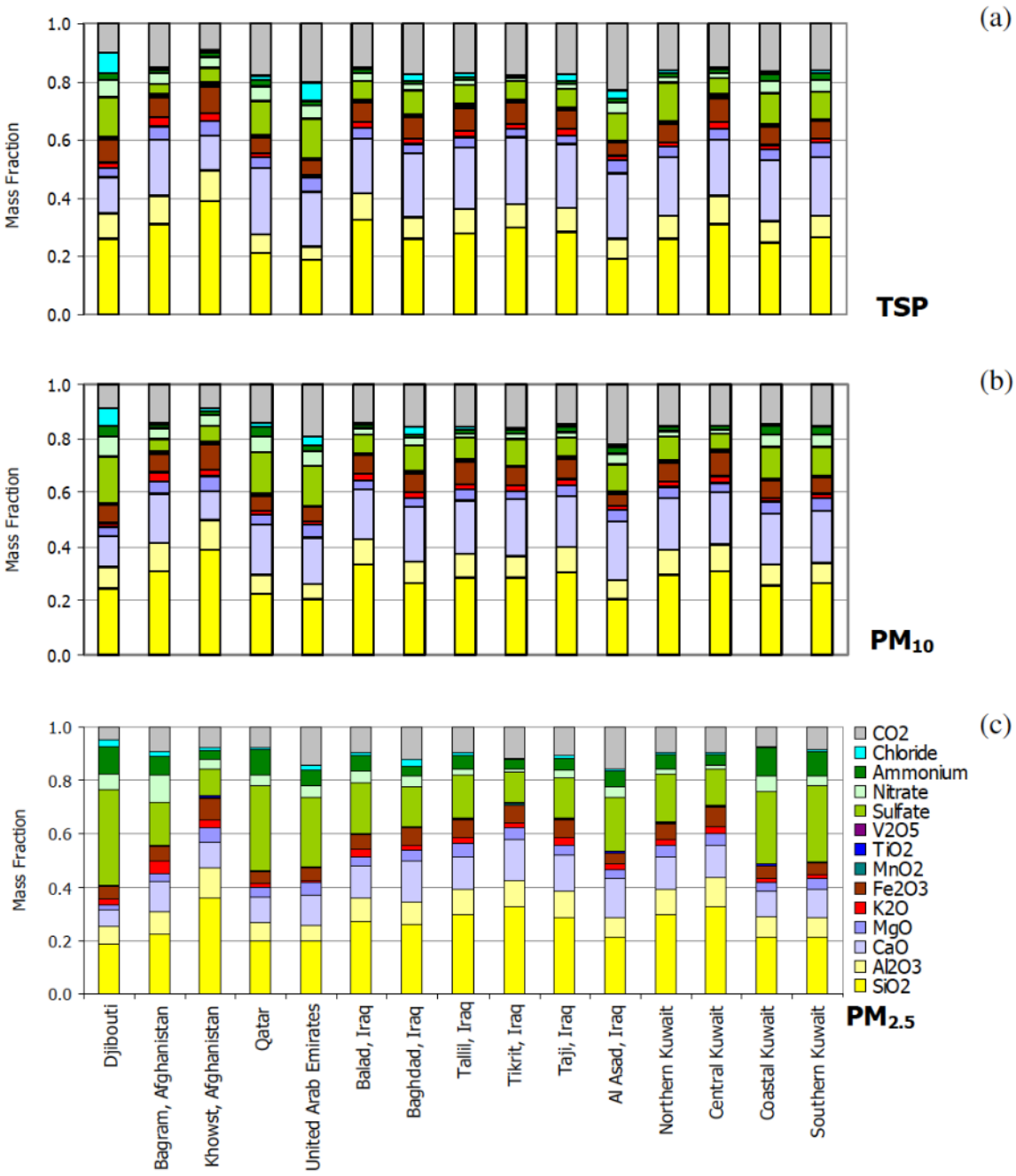

Figure 1. Particulate composition concentration throughout the middle east as mass fractions, (a) TSP, (b) PM10, (c) PM2.5. Source: [8].

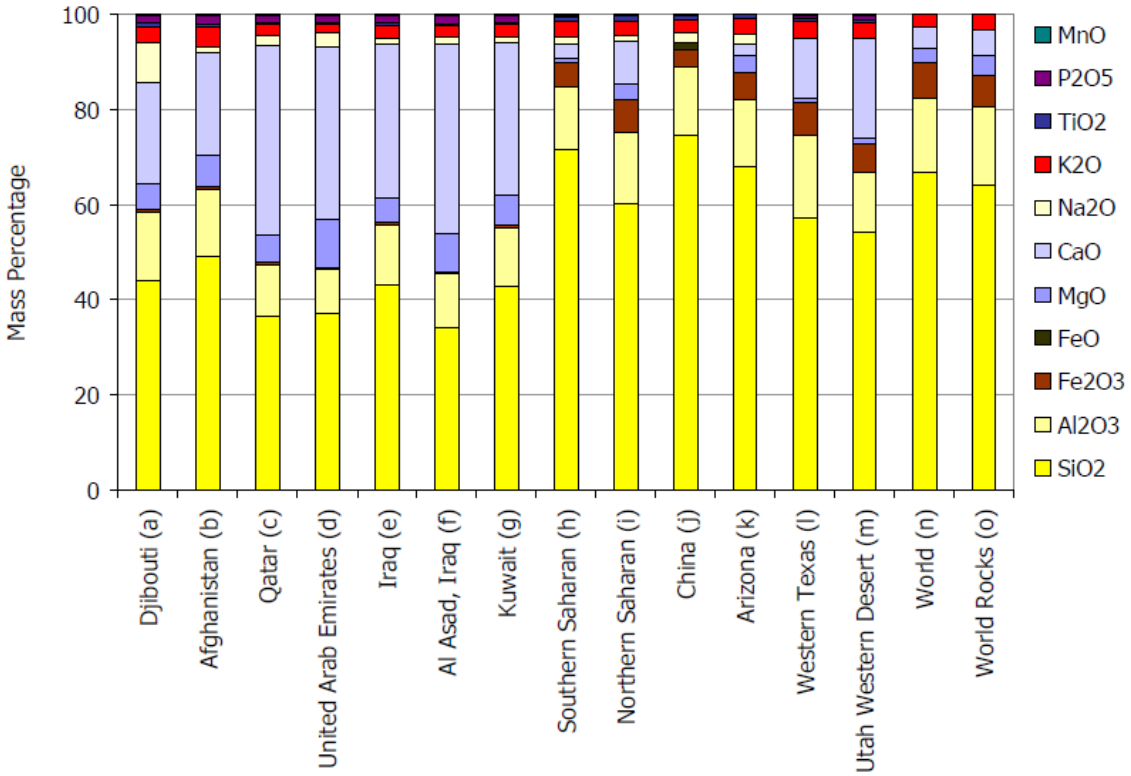

Figure 2. Comparison of composition of dust samples from around the world. Source: [8].

Another study conducted by Kelley et al. [9] evaluated the physical properties of 17 soil samples taken in Iraq and Afghanistan. In both regions the soil was finer than expected, consisting mainly of clay and silt size particles (<0.05 mm) with less sand sized particles (>0.05 mm) [9], [10]. Figure 3 shows a visual comparison of the particle sizes relative to one another, note the scale used is slightly different that that used by Kelley et al. The primary mineral in the Iraq samples was gypsum ($CaSO_4 \cdot 2H_2O$) while the dominant mineral in the Afghanistan samples was calcium carbonate ($CaCO_3$) [9].

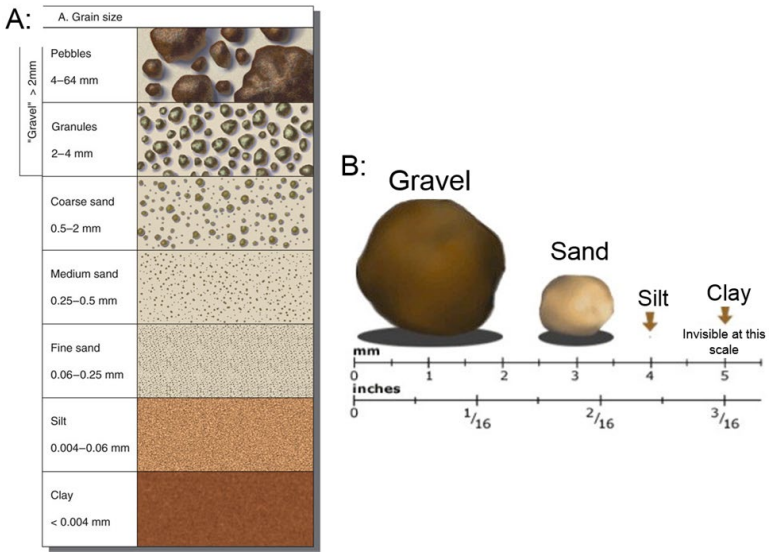

Figure 3. Relative scale of soil grain sizes. Source: [11].

Wet et al. [12] studied sand samples collected from Doha, Dubai, Abu Dhabi, Bahrain, and Sinaiyah airports to analyze the variation in composition and the TBC's reaction to each. They found that although the composition varied by location the most abundant mineral was quartz with varying amounts of calcite, aragonite, dolomite, gypsum, albite, microcline, and diopside [12]. Table 2 shows the general intensities at each location.

Table 2. Mineral intensities of various Middle East locations. Denoted by w=weak, m=medium, s=strong, and vs=very strong. Source: [12].

Mineral	Sinaiyah	Bahrain	Dubai	Abu Dhabi	Doha
Quartz (α-SiO_2)	vs	vs	s	vs	w
Calcite ($CaCO_3$)	w	w/m	vs	s	w
Aragonite ($CaCO_3$)	-	m	-	-	-
Dolomite ($CaMg(CO_3)_2$)	w	w/m	w	w	m
Gypsum ($CaSO_4 \cdot 2H_2O$)	-	-	-	-	vs
Albite ($NaAlSi_3O_8$)	m	w	w	m/s	-
Microcline ($KAlSi_3O_8$)	m	w	w	w	-
Diopside ($CaMg(SiO_3)_2$)	-	w/m	-	-	-

Bansal and Choi [13] took as-received desert sand from the Middle East and heated it into CMAS glass to compare its properties. They found that the as-received sand contained 34% quartz, 11% calcite, 41% gypsum, 7% albite, and 5% Mg-Al silicate phases. After heating the sand to 1400°C, a ~35% reduction in weight was observed which was determined to be caused by the decomposition of calcium $CaCO_3$ and calcium sulfate ($CaSO_4$) [13].

These studies show that although the sand from various regions is generally composed of the same components the density of each varies from sand to sand. One of the steps of GTE design is sand ingestion testing and since it is impractical to gather sand from every sand region throughout the world, a manufactured sand was designed to match the composition of the glass residue collected from attacked turbine blades [11]. As more test and operational service data was collected, a substantial differential in service life between the two was noted. This differential was a result of the manufactured sand not mimicking the naturally found sand close enough. Opie [11] conducted a study to determine which manufactured sand most closely resembled real world sand ingestion. The study determined that Air Force Research Lab-02 (AFRL-02) sand closely simulates real world sand and thus should be used for next generation GTE development [11].

2. CMAS Properties

The viscosity of CMAS is important to understand because it is directly related to how deep the CMAS can penetrate the coating [14]. The lower the viscosity the easier it is to permeate the grain boundaries and work its way deeper into the coating. A key driver of viscosity is the temperature, at higher temperatures there is less internal resistance force within the CMAS thus allowing it to flow easier. To quantify this the Vogel-Fulcher-Tammann equation (1) is used to calculate the viscosity (η). A, B, and T_o are material dependent constants and T is the temperature [14].

$$\log \eta = A + \frac{B}{T - T_o} \tag{1}$$

Thus, as the temperature increases the viscosity will decrease. Table 3 lists some of the common properties of CMAS. The transition, softening, and melting temperatures of

CMAS are significantly below GTE operating temperatures thus creating a prime environment for CMAS infiltration and attack which will be discussed later. The high coefficient of thermal expansion (CTE) also causes problems which will be discussed later.

Table 3. CMAS glass thermal and mechanical properties. Adapted from [14].

Property	**Value**
Density (g/cm^3)	2.63
Glass transition temperature, T_g (°C)	694
Dilatometric softening point, T_d (°C)	751
Melting temperature, T_m (°C)	1176
CTE (25–690 °C), α (K^{-1})	9.32×10^{-6}
Young's modulus, E (GPa)	84.3
Shear modulus, G (GPa)	33.6
Poisson's ratio, v	0.26
Vickers microhardness, H_v (GPa)	6.14±0.1

The XRD peaks in Figure 4 show that CMAS in powdered form is crystalline in nature but once heated into glass, it becomes amorphous, as shown by the lack of distinct peaks in Figure 5.

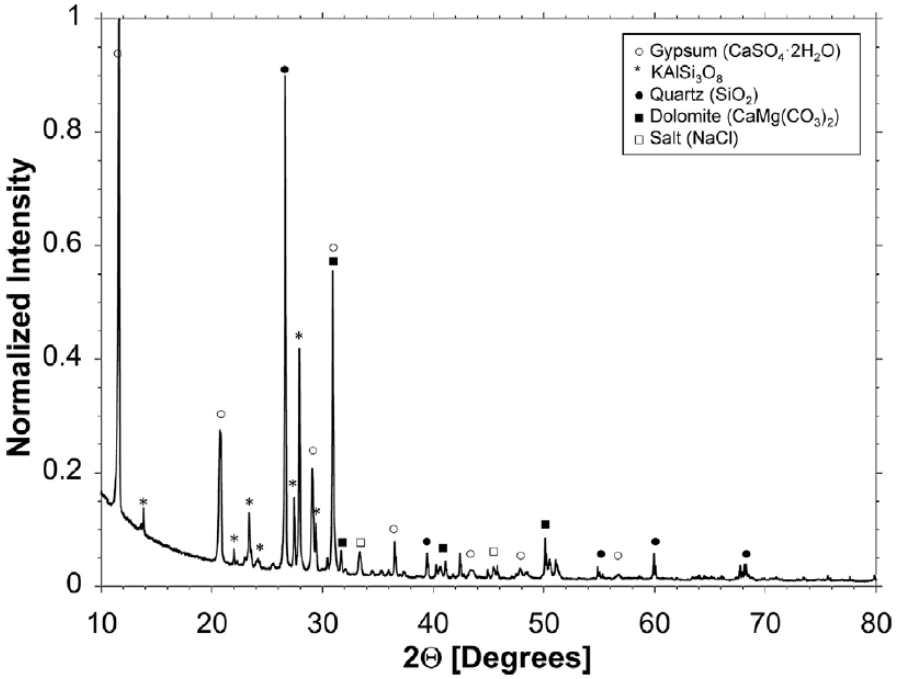

Figure 4. XRD of synthetic as-received CMAS powder. Source: [14].

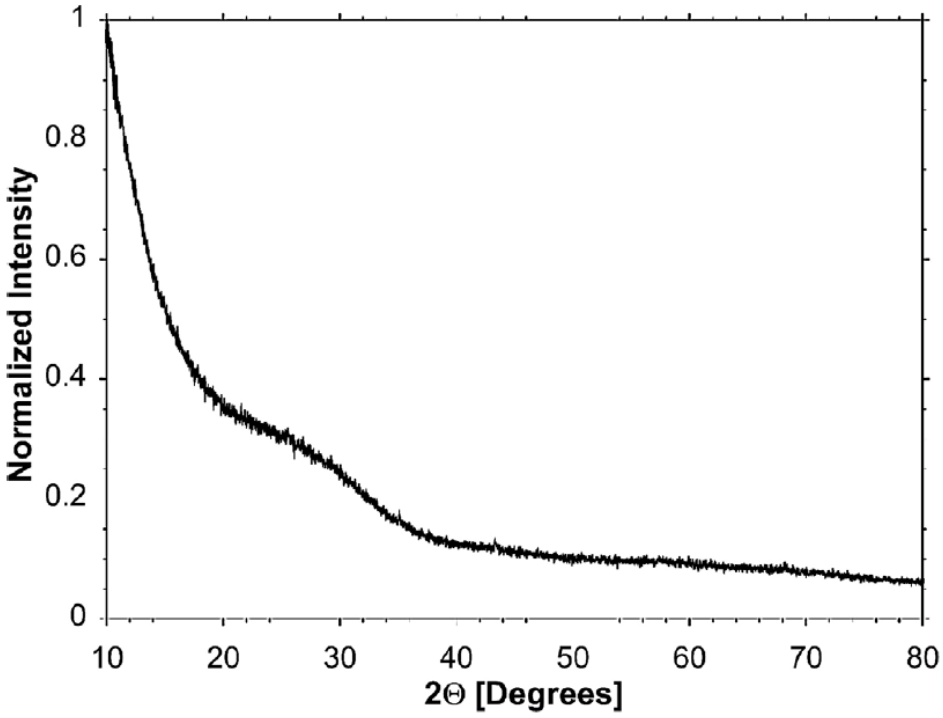

Figure 5. XRD spectra of amorphous CMAS glass. Source: [14].

3. Gas Turbine Coatings

Despite the impressive properties of today's superalloys. They cannot handle the temperatures of today's GTEs. Since the operating temperatures are usually higher than the melting temperature of the superalloy, the GTE components require a thermal barrier to protect the engine components. Some high temperature ceramics like YSZ, are the materials of choice for these coatings due to their high melting temperatures as well as possessing the properties displayed in Table 4. The low thermal conductivity of ceramic coatings helps to improve thermal shock resistance of the component by breaking up the thermal stresses [15]. A critical factor in the effectiveness of the T/EBCs is their endurance and resistance to imperfection/flaw propagation. These flaws provide infiltration pathways through the coating, exposing the substrate. Studies have shown that internal blade stress can be tied to deposition regions along the vane, predominantly occurring near the blade's leading edge cooling holes where the blade has the highest exposure to heat and foreign matter [6].

Table 4. Properties desired for T/EBC materials. Source: [16].

Property	Requirement	Rationale
Melting point	High	Operating environment at high temperature
Thermal conductivity	Low	Temperature reduction inversely proportional to thermal conductivity
Coefficient of thermal expansion	High	Expansion should be close to that of superalloy substrate and bond coats on which coatings are deposited
Phase	Stable	Phase change in thermocyclic environment is structurally detrimental
Oxidation resistance	High	Operating environment highly oxidizing
Corrosion resistance	Moderate to high	Operating environment may be corrosive
Strain tolerance	High	Operating environment imposes large strain ranges

To meet all the required properties mentioned in Table 4, ceramic compounds are used. A commonly used one in today's engines is YSZ. The addition of the seven-weight percent (wt.%) YSZ provides a better coefficient of thermal expansion across more temperatures [16]. Seven wt.% is used because it will maintain the preferred tetragonal structure where lower and higher Y_2O_3 concentrations will transition to monoclinic and cubic phases, respectively. The tetragonal structure is the desired state due to its better durability and strain tolerance compared to the other phases [17].

4. CMAS Attack

During operation in a sandy environment, CMAS particulates enter the GTE making their way to the hot section of the engine. The very high temperature of the hot section melts the CMAS particles. Once molten the CMAS particles have a low viscosity, which allows them to penetrate the T/EBC. The higher the temperature, the less time is needed for infiltration. Once the engine is secured, the molten CMAS cools and solidifies into glass impacting the mechanical and chemical properties of the coating [14]. Figure 6 shows the degradation of an engine vane from operating in sand rich air of the Persian Gulf.

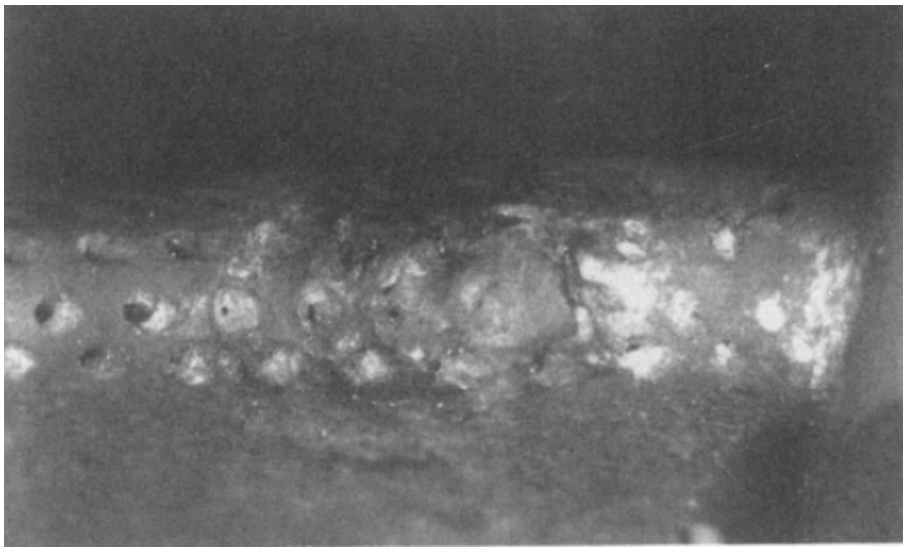

Figure 6. Leading edge of X-40 vane from a helicopter operating in the Persian Gulf. Source: [6].

At elevated temperatures, the current coating materials are unable to inhibit molten CMAS penetration. Figure 7 shows how molten synthetic and volcanic CMAS can penetrate through the T/EBC. This creates problems, because as the CMAS cools and solidifies it causes residual stresses within the coating. These stresses inhibit the coating's ability to counteract the variation in thermal expansion between the coating and composite material beneath it. This eventually leads to coating delamination and failure of the CMC material [14]. The cyclic heating and cooling of the components caused by the normal operation of the GTE makes the problems worse and results in non-ideal mechanical and thermal properties. Mismatch in the coefficients of thermal expansion reduces T/EBC's ability to handle residual stress after cooling resulting in engine component failure [14]. Initiating CMAS crystallization before it can infiltrate the coating is being considered as a viable mitigation technique against CMAS attack. For this to work; however, the crystallization rate needs to be faster than the infiltration rate of the molten CMAS [7].

In a 2021 paper, Guo et al. [3] analyzed how surface roughness affects bulk samples susceptibility to CMAS corrosion. As fabricated and polished bulks were exposed to CMAS corrosion at 1250°C for 1 and 4 hours and it was found that the polished samples experienced less wettability and spreading of the CMAS caused by a reduction in the capillary force [3].

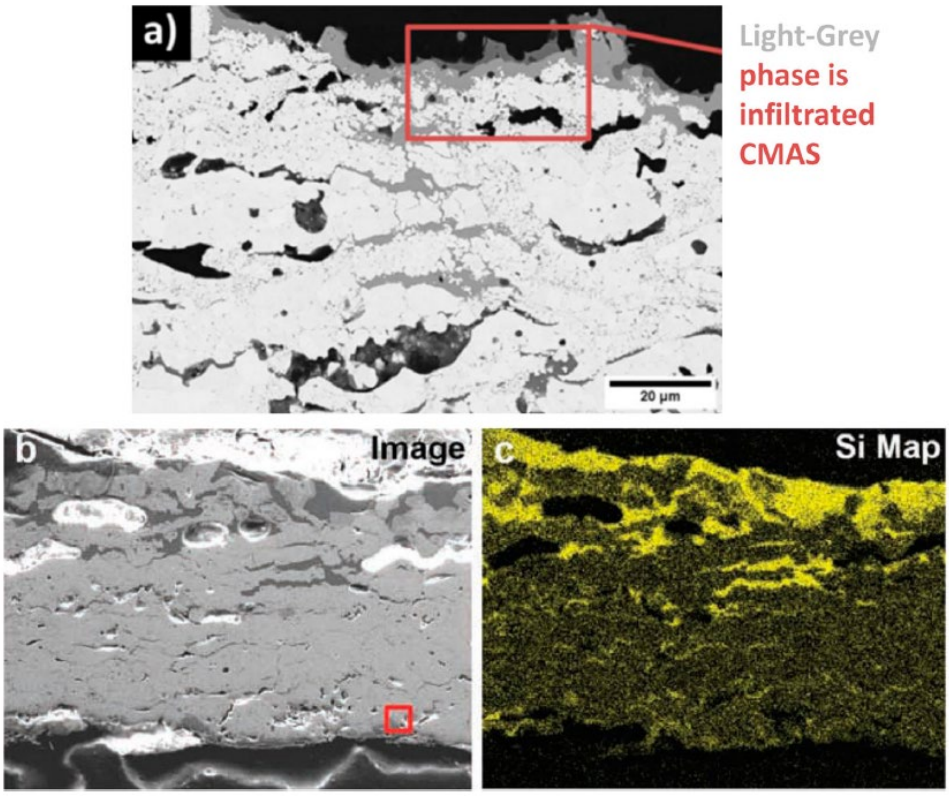

Figure 7. (a) SEM of TBC showing infiltration and coating defects after exposure to synthetic CMAS at 1250°C, (b) TBC after volcanic ash exposure at 1200°C, (c) EDS map of Si in (b). Source: [18].

5. Infiltration and Failure

GTEs force a substantial amount of air through them during operation. This allows the CMAS sand particles in the air to be deposited throughout the engine, primarily in the hot section. As the engine continues to operate the particles melt and wet the T/EBC which leads to infiltration, this infiltration leads to coating experiencing phase transformations and destruction of the coating microstructure, in turn, leading to T/EBC failure [3]. With current T/EBC materials such as YSZ a key contributor to CMAS induced failure is the temperature, being high enough to cause the ZrO_2 and Y_2O_3 to melt into the CMAS. Given that the YSZ has significantly more Zr than Y, the ZrO_2 will begin to precipitate out of the melt before the Y_2O_3. Additionally, the Y_2O_3 is highly soluble in CMAS, meaning the ZrO_2 will lose Y_2O_3. As previously discussed YSZ loses its stabilization effects when the Y_2O_3 is below seven wt.% which means that instead of the desired tetragonal phase, a monoclinic

phase forms within the T/EBC [3]. The molten CMAS, now richer in Y_2O_3, forms cubic ZrO_2 as it cools. The rounded globules shown in Figure 8 are cubic ZrO_2 which formed due to the high concentration of Y_2O_3 that dissolved into the molten CMAS during operation [18].

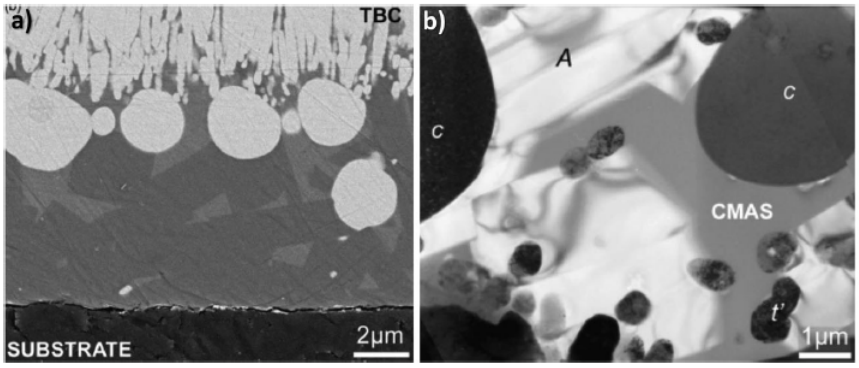

Figure 8. Coatings exposed to CMAS at 1300°C for 4 hours, (a) Multiple phases observed at coating/substrate interface, (b) TEM of aluminosilicate (A), cubic (C) ZrO_2, and tetragonal YSZ (t′) phases. Source: [18].

B. HAFNIUM DIBORIDE AND ZIRCONIUM DIBORIDE LITERATURE REVIEW

1. HfB_2/ZrB_2 Properties

HfB_2 and ZrB_2 are known as refractory diborides due to their high resistance to wear and heat. They are desirable because their properties are easily tailorable when mixed with other transition metals where they form partial or complete solid solutions. When analyzing borides, an important characteristic to look at is the boron to metal ratio which ranges from 1:4 up to 1:12. This is important because as the number of boron atoms increases, the strength and stiffness also increases along with the hardness and chemical stability. Both HfB_2 and ZrB_2 have hexagonal crystalline structures like what is shown in Figure 9 [19]. Since they are both diborides their thermal stability and hardness are dictated by the strength of the metal-boride and the boride-boride bonds. ZrB_2 and HfB_2 have some of the strongest boride-boride bonds and highest hardness within their element groups [19].

Keihn and Keplin's study of HfB_2 and ZrB_2 showed that when subject to rapid cooling they develop lower internal stress than other diborides [20].

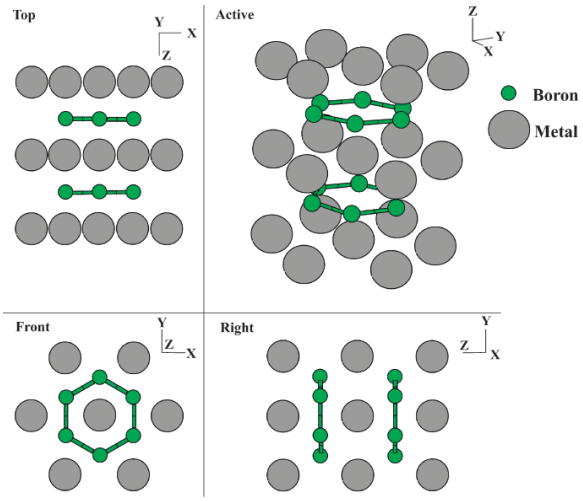

Figure 9. Generic diboride crystalline structure example. Taken from the Center for Computational Materials Science of the USN Research Laboratory's Crystal Lattice Structures Web page. Source: [19].

ZrB_2 is a promising candidate for ultra-high temperature uses because it has a melting temperature above 3000 °C. The diboride maintains its strength at higher temperatures and has a high thermal conductivity. It also has high electrical conductivity and good chemical stability. Unfortunately, it has a low fracture toughness and is subject to thermal stress induced catastrophic failure (i.e., low thermal shock resistance) [15], [19], [21]. ZrB_2 ceramics tend to be brittle and sensitive to cracks. One method of ceramic healing that has been tried is the addition of elements such as aluminum or silicon to the ceramic to increase its reliability [22]. However, these additions lead to oxidation, which will be discussed later in this section.

Table 5 shows the common properties of HfB_2 and ZrB_2. One property of particular interest is the hardness, note the variations between the types of hardness tests and the range of hardness across the test. The range in the Vickers hardness is largely due to the varying densities of the tested samples, the less dense samples had lower hardness while the fully dense (>99%) samples had higher hardness [23]. Bazhin et al. [24] and Shahedi

Asl et al. [25] in separate studies showed that the nano hardness varied with structure, the less crystalline and more amorphous a structure the higher the nano hardness.

Table 5. Mechanical properties of HfB_2 and ZrB_2.

Property	**HfB_2**	**ZrB_2**	**Source**
Density, ρ (g/cm^3)	11.212	6.119	[19]
Melting temperature (°C)	3380	3245	[19]
CTE, α (K^{-1})	6.3×10^{-6}	5.9×10^{-6}	[19]
Young's modulus, E (GPa)	480	489	[19]
Poisson's ratio, ν	0.16	0.16	[19]
Vickers hardness, H_v (GPa)	28-32.9	16.7-23	[19], [23], [26]
Nano hardness, H_b (GPa)	13-44	10-24.8	[24], [25]

One obstacle standing in the way of widespread use of ZrB_2 and HfB_2 is their poor sinterability and densification. Several factors contribute to this to include: strong covalent bonding, low self-diffusion coefficient, large particle size, and surface oxide contamination [27]. To achieve the desired densification, current processes utilize a combination of grain size refinement and sintering additives. Grain size refinement is usually achieved by wet attrition milling to achieve sub-micron grain sizing. There is greater variation in the types of sintering additives used but they fall into either the reactive agent or liquid phase former categories [27]. The sintering additives currently being used are varying ratios of B/C powders, tungsten carbide (WC), molybdenum disilicide ($MoSi_2$), hafnium nitride (HfN), silicon nitride (Si_3N_4), and SiC [28]–[30].

2. UHTCs

ZrB_2 and HfB_2 along with other carbides and nitrides of the group IV and V transition metals make up the group of materials known as ultra-high temperature ceramics (UHTCs). They are known as UHTCs because their melting temperature exceeds 3000°C [19]. In addition to high melting temperatures these materials exhibit good strength, thermal and chemical stability, hardness, and oxidation resistance at elevated

temperatures [31], [32]. Although boride based UHTCs have lower melting temperatures than carbide based UHTCs, they are being explored because of their higher thermal and electrical conductivities and lower CTE resulting in decent thermal shock resistance. Based on current research, borides also seem to have better oxidation resistance than nitrides and carbides [2]. Table 6 compares the thermal properties of common UHTC boride, nitrides, and carbides.

Table 6. UHTC thermal properties. Source: [2].

	Thermal Expansion	Temp. Range	Thermal Conductivity	Temp.	
Material	10^{-6}/K	°C	W/m*K	°C	Ref.
HfB_2	6.3	20–1027	105	20	5, 30
	6.8	1027–2027	75	400	5, 30
	7.6	20–2205	70	800	5, 30
HfB_2-20v% SiC	–	–	79	100	31
	–	–	74	500	31
	–	–	62	1000	31
HfC	6.6	20–1500	20	20	5
	–	–	23	400	5
	–	–	30	800	5
HfN	~6.5	20–1000	18	20	5
	–	–	20	400	5
	–	–	22	800	5
ZrB_2	5.9	20–1027	–	–	30
	6.5	1027–2027	–	–	30
	8.3	20–2205	–	–	30
ZrB_2-20v% SiC	5–7.8	400–1600	98.7	100	31
	–	–	84.5	500	31
	–	–	78	1000	31
ZrC	6.7	20–1500	–	–	25
TiB_2	4.6	20–1027	–	–	30
	5.2	1027–2027	–	–	30
	8.6	20–2205	–	–	30
TiC	7.7	20–1500	–	–	25
TaB_2	8.2	20–1027	16.0	20	30
	8.4	1027–2027	16.1	1027	30
	8.4	20–1650	36.2	2027	30
TaC	6.3	20–1500	–	–	25
SiC	1.1	20	114	20	32
	5.0	1000	35.7	1000	32
	5.5	1500	26.3	1500	32

3. Oxidation

Oxidation is the process by which oxygen chemically reacts with a material resulting in the formation of oxides. Diborides when exposed to air at elevated temperatures experience stoichiometric oxidation. The coefficient of thermal expansion of the oxides is different than the diborides which leads to thermal mismatch eventually resulting in material failure of the coating. The primary oxidation products of HfB_2 and ZrB_2 are HfO_2 (hafnia) and ZrO_2 (zirconia), respectively, as well as B_2O_3 (boric oxide). Additionally, there is some evidence of HfSiO4 (hafnon) and ZrSiO4 (zircon) forming at elevated temperatures [5], [33]. Equations (2) and (3) show the standard oxidation reactions of each material.

$$HfB_2(c) + \frac{5}{2}O_2(g) \rightarrow HfO_2(c) + B_2O_3(l) \tag{2}$$

$$ZrB_2(c) + \frac{5}{2}O_2(g) \rightarrow ZrO_2(c) + B_2O_3(l) \tag{3}$$

Oxidation is of substantial interest in T/EBC because at elevated temperatures oxidation occurs at different rates and the oxides undergo solid-phase transformations resulting in temperature dependent changes of volume as shown in Table 7 [34]. These phase changes can potentially play a role in the premature failure of the T/EBC. One oxidation resistance technique is the addition of silicon carbide (SiC) particles to the ceramic. The addition of these particles promote silicate-based glass formation which inhibit oxidation between 800 and 1700°C [22].

Table 7. Phase change temperature of ZrO_2 and HfO_2. Adapted from [34].

	Monoclinic →Tetragonal (°C)	Tetragonal →Cubic (°C)
HfO_2	1650	2700
ZrO_2	1150	2370

One factor influencing the oxidation rate of HfB_2 is one of the products of the oxidation reaction: boric oxide. Tandon et al. [32] found that HfB_2 shows increased oxidation resistance below the boiling point of boric oxide at 1500°C. Since the boric oxide is a liquid below 1500°C it penetrates the voids on the surface of the HfB_2 thus sealing the voids and preventing oxygen from penetrating the sample further to continue the oxidation process. Above 1600°C HfB_2 displays poor oxidation resistance due to the boiling of the boric oxide. Addition of molecules containing carbon such as hafnium carbide (HfC) or SiC help protect the material surface from oxidation due to the continuous formation of carbon monoxide (CO) which helps promote escape of the boric oxide [32]. Figure 10 shows the microstructural differences of the oxidation occurring at different temperatures.

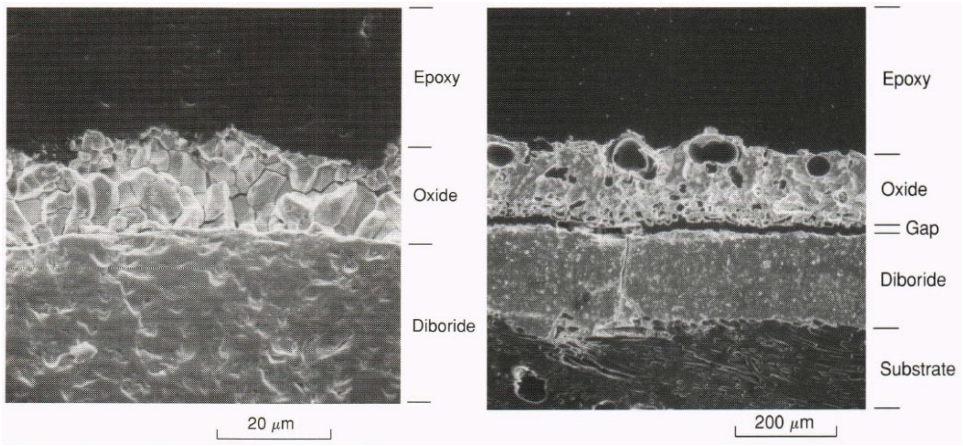

Figure 10. Cross sections of oxidized HfB_2 (a) 1520°C for 1800 s, (b) 1900°C for 300 s. Source: [35].

As seen in equation 3, ZrB_2 has a similar oxidation reaction to HfB_2 with the oxidation resulting in ZrB_2 and B_2O_3. The amount of each phase is dependent on the temperature. Parthasarathy et el. [36] modeled ZrB_2 oxidation behavior from 1000°C to 1800°C showing that the phase distributions fall into three temperature ranges. Below 1000°C, a glassy boric oxide film forms on top of the oxidation scale. Since it is a continuous layer, it provides passive oxidation protection. As the temperature increases the zirconia microstructure transforms from equiaxed grains to more columnar in shape. At intermediate temperatures, 1000°C to 1800°C, the vacancy between the grains is filled by

the liquid B_2O_3, which regulates the rate of oxidation. Mass change in this zone is a combination of mass gain from oxide formation and mass loss from the B_2O_3 formation. As the temperature increases, the liquid B_2O_3 completely boils, which allows the ZrO_2 grains to interact with the surrounding oxygen thus increasing the oxidation rate. Once the boiling temperature of B_2O_3 is surpassed, the sample experiences linear mass gain from the oxides [19], [36], [37]. Figure 11 shows the oxidation behavior across the three temperature zones. Table 8 summarizes HfB_2 and ZrB_2's oxidation products.

Table 8. Summary of Oxidation Products of HFB_2 and ZrB_2. s=solid, l=liquid, g=gas. Adapted from [5].

Compound	Temperature (°C)	Products
HFB_2	above 1215	HfO_2 (s); B_2O_3 (g)
ZrB_2	below 1056 above 1165	ZrO_2 (s); B_2O_3 (s, l) ZrO_2 (s); B_2O_3 (l, g)

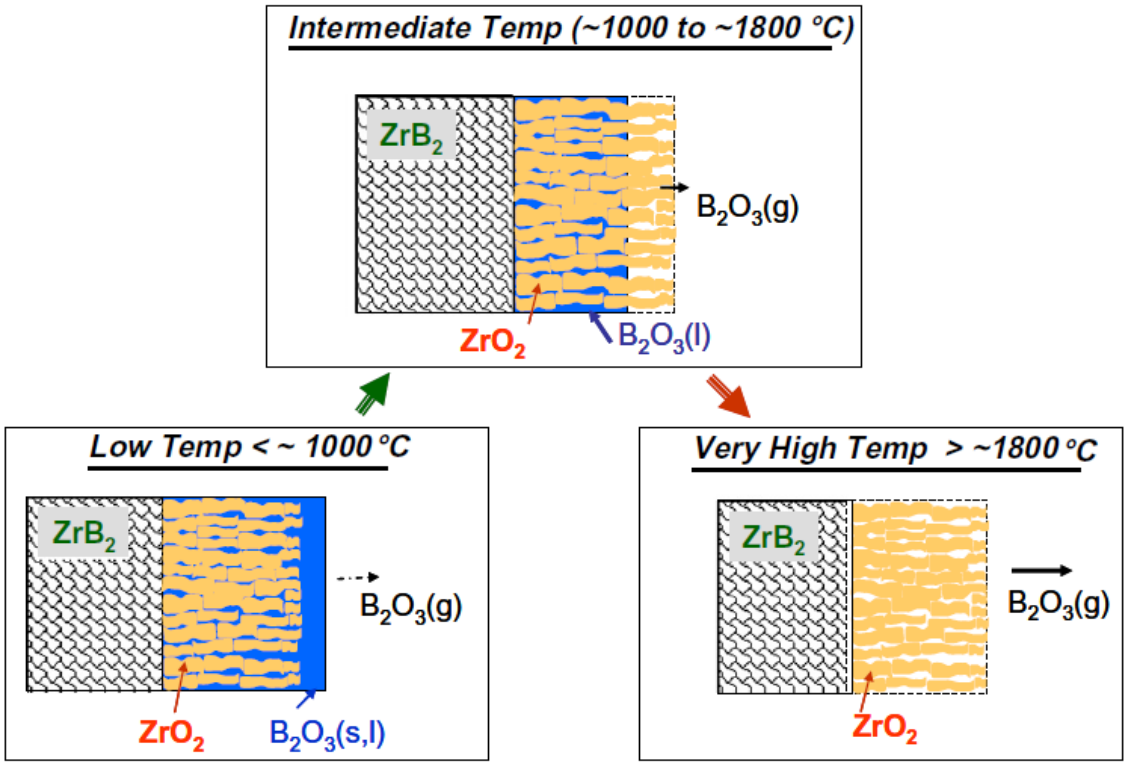

Figure 11. ZrB_2 oxidation during three temperature regimes. Source: [36].

C. HIGH ENTROPY BORIDES LITERATURE REVIEW

1. HEB Composition

High entropy materials have become an area of substantial research interest in recent years. One reason they are being explored for use in ultra-high temperature environments is high entropy materials have lower Gibbs free energy resulting in higher thermal stability [38]. Along with Zr and Hf; Ti, Nb, and Ta also forms stable AlB_2 diboride compound structures, as shown in Figure 9, making them good candidates for material property tailoring [2]. High entropy borides (HEB) are being explored for use in high temperature and extreme environments because of their impressive mechanial and physical properties. HEBs consist of the following composition: $Hf_{0.2}Zr_{0.2}Ta_{0.2}M_{0.2}Ti_{0.2}B_2$; M = Nb, Mo, Cr. HEBs are typically made by high energy ball milling the raw precursor borides then spark plasma sintered at 2000°C [39]. Research shows that when crystallized HEB forms a hexagonal layer structure, see Figure 12, with the boron atoms being covalently bonded while the metal atoms are a combination of ionic and covalent bonds.

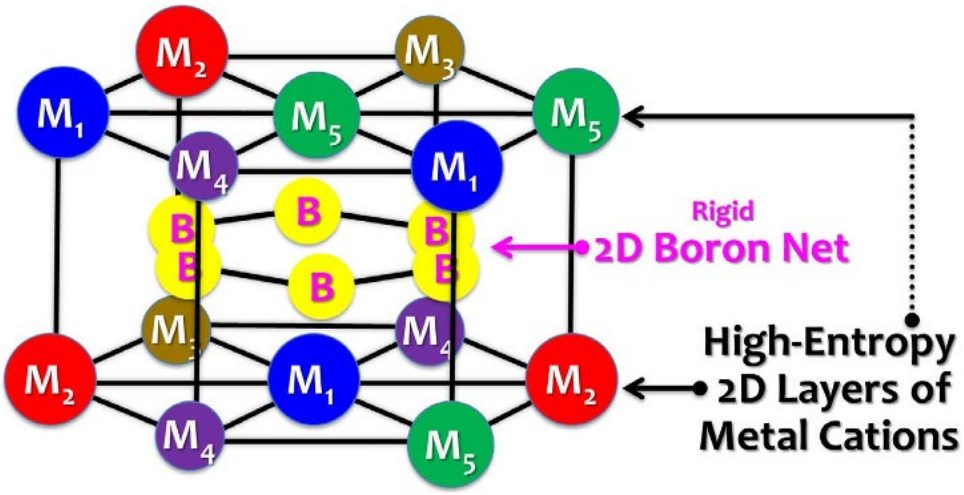

Figure 12. Atomic structure of HEBs. $M_{1\text{-}5}$ represent the five transition metals composing the HEB. Source: [40].

The larger configurational entropy of the five constituent elements, as opposed to small amounts of minor alloying elements added to a primary metal like chromium to iron

for stainless steel, helps the solid solution phase to stabilize thus preventing the formation of intermetallic compounds [41]. The HEB that this work focuses on has a hexagonal crystal structure. This crystal structure allows the various transition metals to substitute with each other resulting in lattice distortion and an increase in the energy barrier leading to increased hardness [38]. Gild et al. [40] observed that HEBs had lower relative densities than binary borides processed by identical sintering conditions. The lower density means more voids and vacancies between grains which could serve as infiltration pathways for external particles such as CMAS.

2. HEB Properties

Hf, Zr, Ti, Nb, and Ta have similar sized radii, differing by less than 10%, they form continuous solid solutions with one another [19]. This is beneficial in ensuring uniform element distribution within the sample leading to more uniform material properties and behavior [39]. Figure 13 shows this uniform element distribution throughout the material. However, variations in the anisotropy and strain in the solid solution can impact the cohesion strength of the grain boundary [19]. Reduced grain boundary strength provides less infiltration resistance and could allow molten CMAS to penetrate the material more easily. Qiao et al. [42] studied the fabrication and characterization properties of HEBs finding the nano hardness to be 36.9 ± 2.3 GPa with a Young's modulus of 545 GPa for the experimental Poisson's ratio of 0.178 [42].

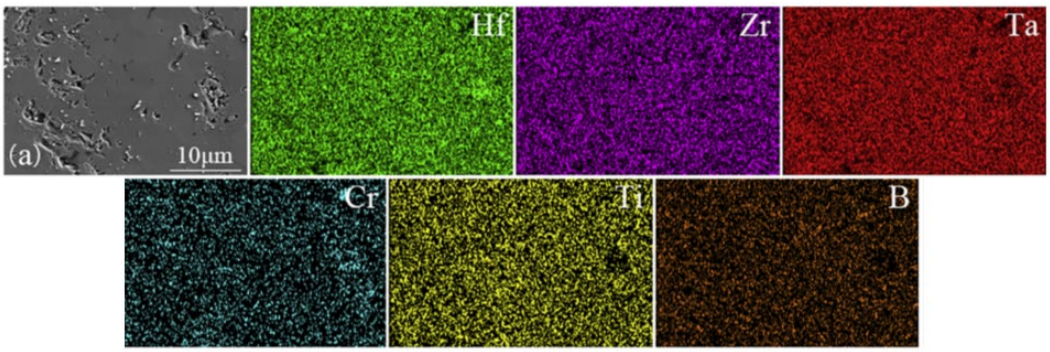

Figure 13. SEM image and corresponding EDS elemental mapping. Adapted from [39].

THIS PAGE INTENTIONALLY LEFT BLANK

III. MATERIALS AND METHODS

A. SAMPLE PREPARATION

1. Spark Plasma Sintering

One of the original methods to achieve densification of diborides is hot pressing, which as the name implies uses a combination of elevated temperature and pressure to overcome the covalent bonds and low diffusion rates. At a temperature above 2000°C this requires 20–30 MPa but if the temperature was below 1850°C it requires a pressure 40–50 times higher than what is required at 2000°C. Even with this temperature and pressure the achievable density was around 95% [19].

A newer densification technique that is like hot pressing utilizes electric current instead of indirect heating to elevate the temperature of the material being densified. This technique is known as Spark Plasma Sintering (SPS) which uses the simultaneous combination of electric current and uniaxial loading to heat and compress the powder. The current is applied to the dies causing them to heat up and providing much faster heating rates, upwards of 100°C/min, which in turn promotes rapid densification preventing excessive grain growth [19]. This allows for a more uniform densification rate over a broader range of temperatures ultimately resulting in a denser material in less time than densification via hot pressing. The current used in heating the dies may break down nonconductive oxides present on the particle surface. HfB_2 ceramics densified via SPS seem to possess less oxide impurities than similar ceramics produced via hot pressing [19]. Used to produce dense ceramics at low temperatures and less time than other methods such as hot pressing. The high energy of the plasma sintering causes surface activation of the particles, local melting, and evaporation between particles [21]. Another possible benefit of SPS is that the plasma created during the process is proposed to have a cleansing effect on the surface thus reducing the amount of oxidation that occurs [43]. To aid in these “cleansing” effects sintering aids are often added to the material prior to sintering. A common sintering aid is carbon which helps the densification and is believed to remove the surface oxides of the ceramic by interfacial reactions [44].

The precursor powders for the materials studied were hand mixed than ball-milled using a high energy ball mill (HEBM) using tungsten carbide lined stainless steel jars and 11.2 mm tungsten carbide milling media. SPS was performed in vacuum, first being held at 1400°C for 80 mins then 1600°C for 80 mins under a 5MPa uniaxial load. This allowed for out-gassing and reduction of native oxides. The temperature and pressure were increased to 2200°C and 80 MPa and held there for 20 mins to allow for densification [41].

2. CMAS Preparation

The CMAS used for this study was AFRL 02 Test Dust (Powder Technology Inc, MN, USA). It is composed of 34% Quartz, 30% Gypsum, 17% Aplite, 14% Dolomite, and 5% Salt [45]. The as-received CMAS was mixed with water at a 1:1 mass ratio.

B. HIGH TEMPERATURE FURNACE TESTING

The samples were placed on platinum (Pt) foil in a ceramic crucible. The CMAS slurry was placed on top of each sample at a concentration of 50 mg/cm^2, the crucible was then placed in a high temperature furnace (CM Furnaces Inc, Bloomfield, NJ, USA), seen in Figure 14. The furnace was programmed to a heating rate of 6 °C/min until the desired test temperature was achieved and maintained that temperature for the designated time. In total 4 different temperature/time tests were performed. 1300°C for 1 and 10 hours and 1600°C for 1 and 10 hours.

Figure 14. CM high temperature furnace.

C. CHARACTERIZATION

1. Microstructure Analysis

In order to analyze the microstructure, the samples were cross sectioned and epoxy mounted then ground and polished using a Buehler ECOMET 4 variable speed grinder-polisher (Lake Bluff, Illinois, USA) with 240, 400, 600, 800 grit sandpaper then polished with a napless cloth using 3 and 1 micron diamond silicas and finished with colloidal silica on a napped cloth for 1–5 minutes [46]. The polisher was set to 220 rpm with 18–22 pounds of force utilizing the counter rotating head and platen setting.

An AmScope SF-2TRA Stereo Microscope (Irvine, California, USA) was used to estimate the size and percentage of the phases present in the boride samples after infiltration by the CMAS. Helios 5 scanning electron microscope (SEM) (Thermo-Fisher Scientific, Hillsboro, OR, USA) was used to image the microstructure of the cross sectioned samples.

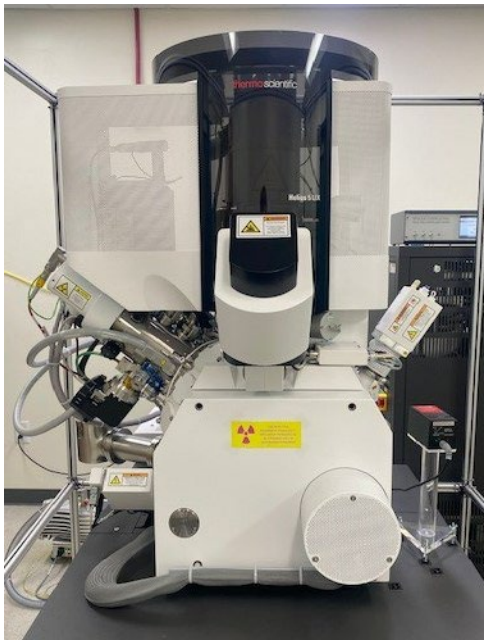

Figure 15. Helios 5 scanning electron microscope.

2. X-ray Diffraction

The samples were ground to a fine powder using an SFM-8 Agate mortar automatic grinder so that they could analyzed with powder X-ray diffraction (XRD). A Rigaku MiniFlex 600 XRD machine (Rigaku, Tokyo, Japan) with Cu Ka radiation was used for spectra analysis of the samples. A 2θ angle from 10 to 100° was analyzed utilizing a step size of 3°/ min and power settings of 40kV and 15mA.

Figure 16. Rigaku MiniFlex 600 X-Ray diffraction.

3. Nano Hardness

Nano hardness testing was done instead of micro hardness for multiple reasons. First, nano hardness allowed for more testing along the cross section of the sample and better delineation between the unaffected, transition, and affected zones within the sample. The other reason nano hardness was chosen was that it can better depict the theoretical hardness by being able to avoid porosity and sample impurities during testing [42]. An Agilent Technologies (Santa Clara, California, USA) G200 nano indenter set at a max load of 40 gf, 5 second peak hold time, and a 10 second time to load was used. Poisson's ratios of 0.178, 0.16, and 0.16 were used for the HEB, HfB_2, and ZrB_2 respectively [19], [38].

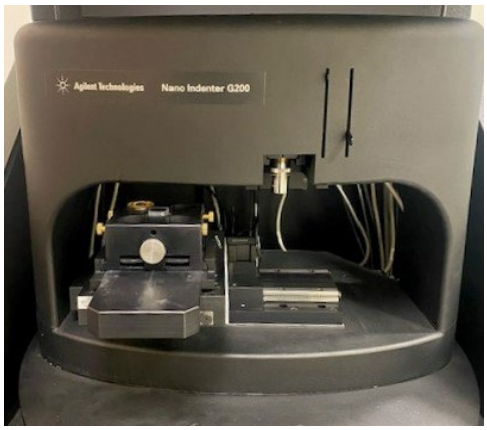

Figure 17. Agilent Technologies G200 Nano Indenter.

THIS PAGE INTENTIONALLY LEFT BLANK

IV. RESULTS

For tracking purposes, each sample was given an alphanumeric label based on the material type and exposure time. This nomenclature is explained in Table 9 and will be used throughout the results sections.

Table 9. Test sample nomenclature.

Temperature (°C)	**1600**	**1600**	**1300**	**1300**	**n/a**
Time (hours)	**1**	**10**	**1**	**10**	**n/a**
(Ta,Zr,Nb,Hf,Ti)B_2 High Entropy Boride (~97% RD)	B1	B2	B3	B4	B5
HfB_2 (~99% RD)	H1	H2	H3	H4	H5
ZrB_2 (~97% RD)	Z1	Z2	Z3	Z4	Z5

A. PRE-MOUNTING IMAGERY

Before the samples were epoxy mounted for analysis, they were imaged at low magnification. Since the test samples weren't identical in shape, this allowed for easier comparison and an initial estimation of the sample's resistance performance. Figure 18 shows the as-received control samples that were not exposed to heat or CMAS. Even though the samples were all produced by the same technique, SPS, they had different surface finishes. The HEB and ZrB_2 samples had mirror like finishes while the HfB_2 samples had a rougher, more "matte"-like finish. As mentioned in Table 9 the HEB and ZrB_2 samples had a slightly lower relative density (97%) than the HfB_2 samples (99%).

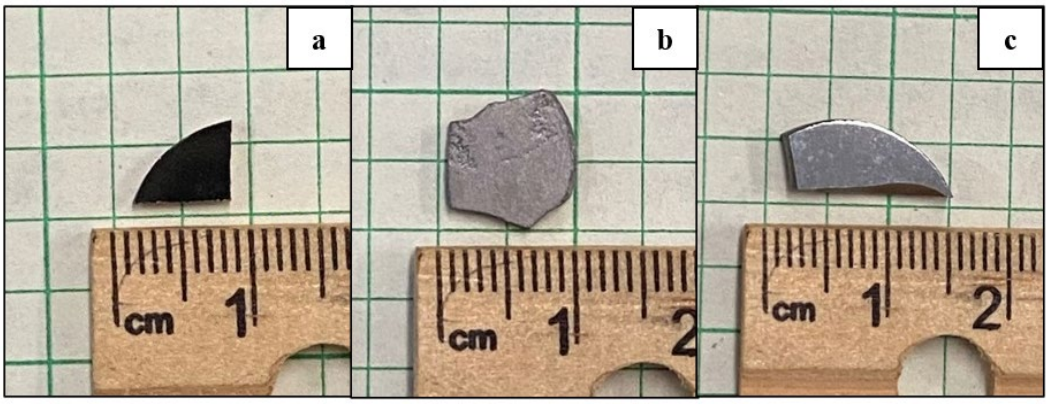

Figure 18. Control sample pre-mounting images: (a) HEB (B5), (b) HfB_2 (H5), and (c) ZrB_2 (Z5).

The CMAS resistance at 1300°C varied across the samples. On preliminary visual inspection, Figures 19 and 20, showed that the HfB_2 and ZrB_2 samples appear to resist CMAS infiltration with a shiny, glassy residue forming on the surface. The metal diboride samples with 10 hours of exposure at 1300°C (H4 and Z4) visually appeared to be degraded but still retained a small glass layer. The HEB samples appeared to show less resistance to CMAS attack. After 1 hour of exposure time, the CMAS glass is visible on the surface of the HEB sample but significantly duller in appearance than the CMAS glass observed on the metal diboride samples. Visual inspection of the 10 hour test sample (B4) shows no signs of CMAS glass. The surface of B4 appears more porous than the other samples treated at 1300°C for 10 hours.

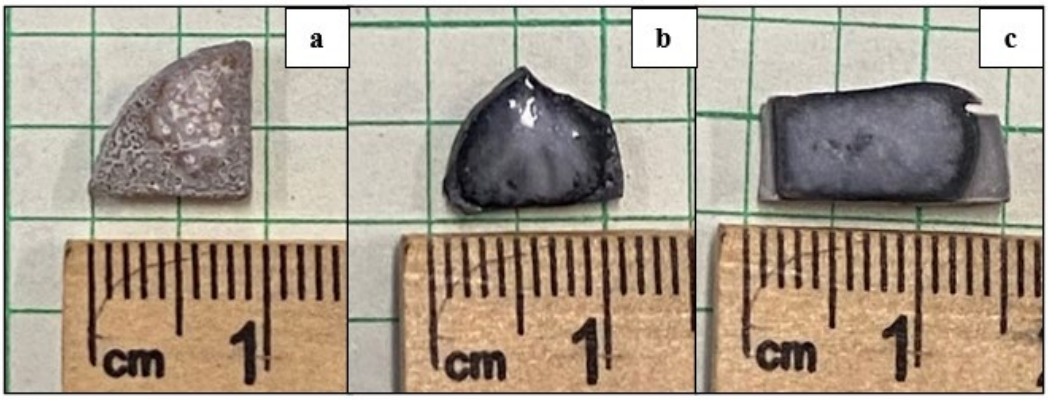

Figure 19. 1300°C for 1 hour pre-mounting images: (a) HEB (B3), (b) HfB_2 (H3), and (c) ZrB_2 (Z3).

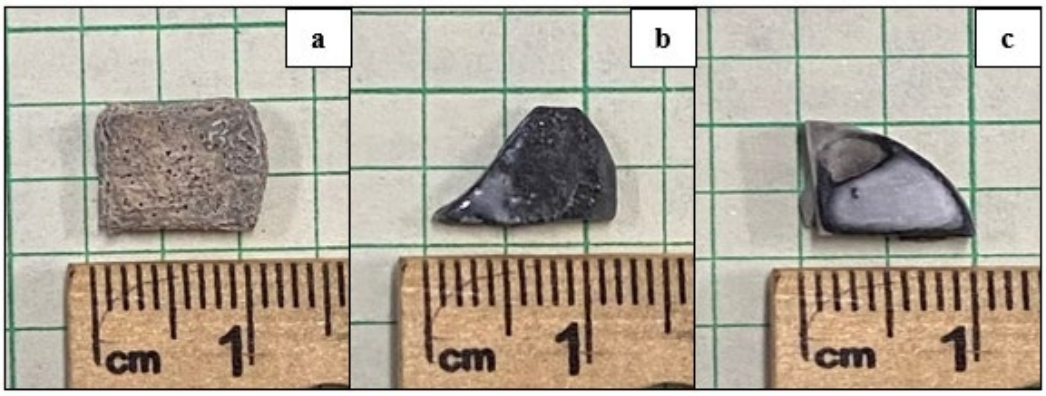

Figure 20. 1300°C for 10 hours pre-mounting images: (a) HEB (B4), (b) HfB_2 (H4), and (c) ZrB_2 (Z4).

The 1600°C samples, Figures 21 and 22, show significantly more reaction between the CMAS and substrate. Unlike a majority of the 1300°C tests there is no shiny CMAS glass visually present on the surface. After the 1 hour test there was very little of the B1 sample remaining. After the 10 hour test, the B2 sample had experienced total transformation and disintegration leaving only a small ring of residual material on the Pt foil. The HfB_2 and ZfB_2 samples showed greater oxidation than the 1300°C tests but remained close to their original shapes without severe disintegration. Increased oxidation is expected at this temperature because the temperature now exceeds the boiling point of boric oxide. As previously discussed, as the boric oxide evaporates the oxide layer is reduced resulting in decreased oxygen resistance. The oxide layer typically exhibits higher

resistance to oxygen diffusion. It is apparent that more reactions occurred at the higher temperature tests because the material was significantly more brittle than the 1300°C tests.

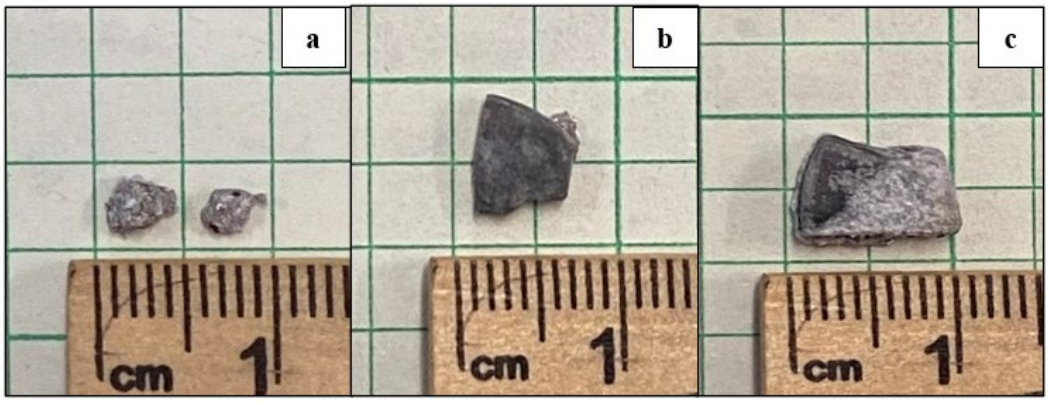

Figure 21. 1600°C for 1 hour pre-mounting images: (a) HEB (B1), (b) HfB_2 (H1), and (c) ZrB_2 (Z1).

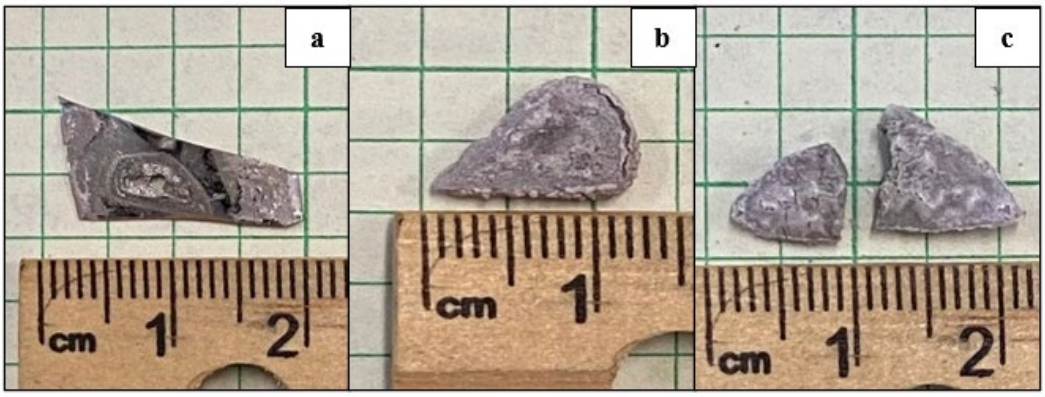

Figure 22. 1600°C for 10 hours pre-mounting images: (a) HEB (B2), (b) HfB_2 (H2), and (c) ZrB_2 (Z2).

B. OPTICAL & STEREO MICROSCOPY

Stereo microscopy was used to approximate the amount of transformation that occurred during the thermal process. Figures 23–25 are stereo and optical images of the cross sectioned control samples. The stereo images were taken at low magnification prior to the samples being polished and the optical images were taken post polishing. Given that these samples were not exposed to CMAS and high heat, there were not significant

observations to be made. One observation is the samples appear relatively uniform. B5 appeared to lack major voids and even exhibited grain structure at these lower magnifications. The H5 and Z5 samples, on the other hand, exhibited a higher void density as compared to B5 with H5 exhibited the highest apparent percent porosity followed by Z5.

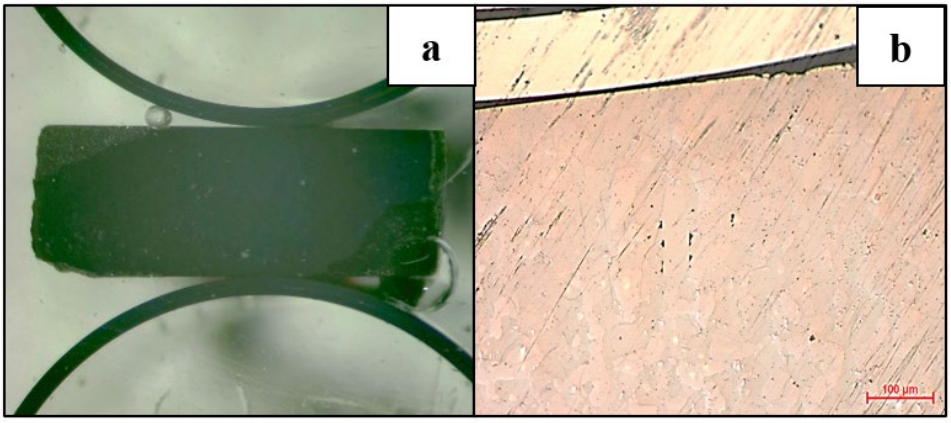

Figure 23. Stereo and optical images of cross sectioned B5 sample, (a) stereo (b) optical.

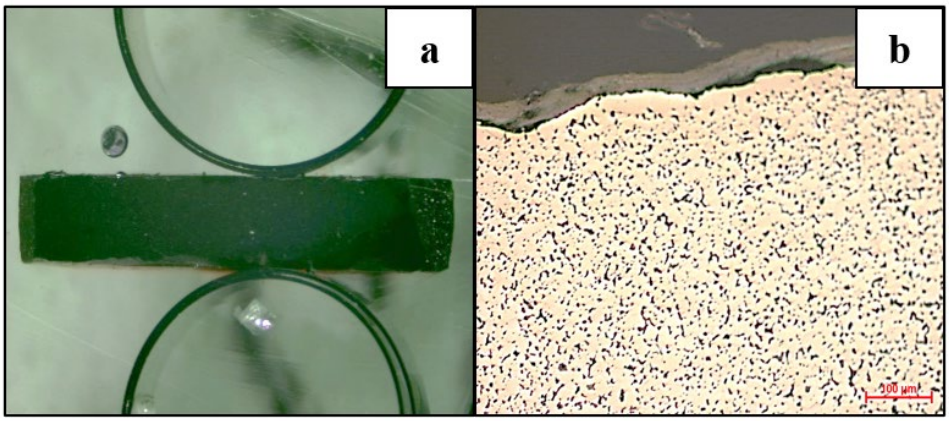

Figure 24. Stereo and optical images of cross sectioned H5 sample, (a) stereo (b) optical.

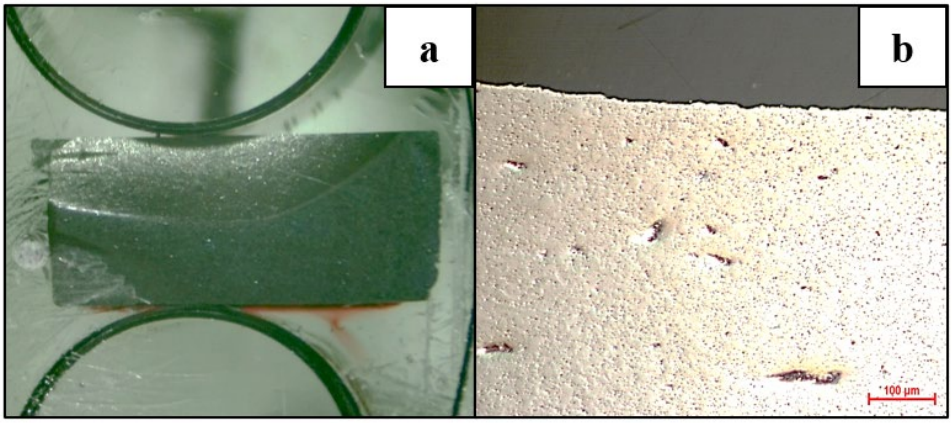

Figure 25. Stereo and optical images of cross sectioned Z5 sample, (a) stereo (b) optical.

Figures 26–28 are the samples exposed to 1300°C for 1 hour. The samples all showed some transformation on the surface but do not appear to have significant CMAS infiltration. The B3 and Z3 samples experienced slightly more transformation than the H3 sample, see Table 10 for the transformation percentages. The CMAS glass scale on the H3 and Z3 samples appears smoother at the surface while the CMAS on the B3 sample is slightly rougher and more porous. This aligns with what was observed on the pre-mounted samples.

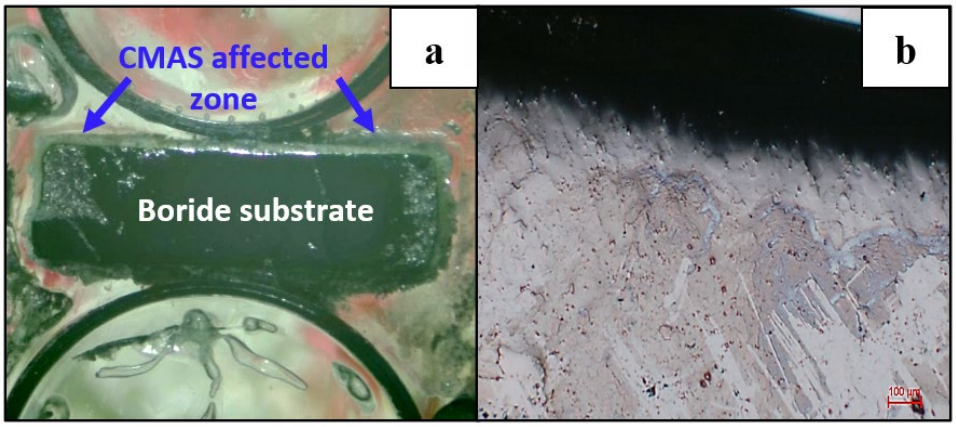

Figure 26. Stereo and optical images of cross sectioned B3 sample, (a) stereo (b) optical.

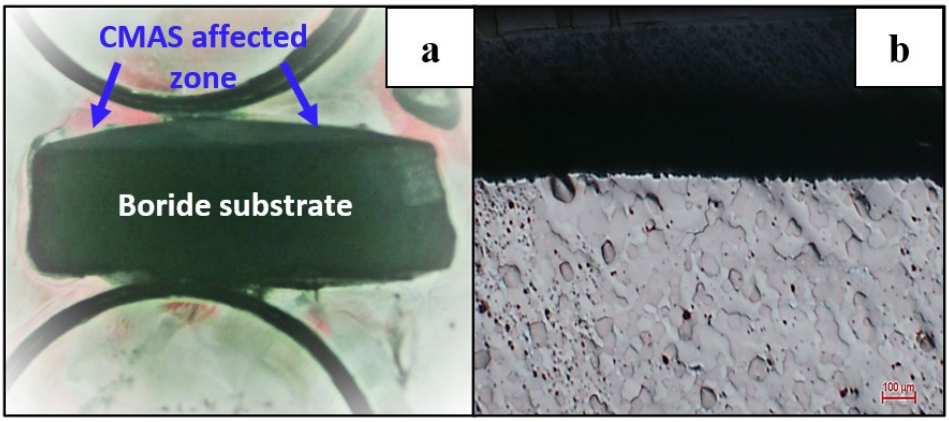

Figure 27. Stereo and optical images of cross sectioned H3 sample, (a) stereo (b) optical.

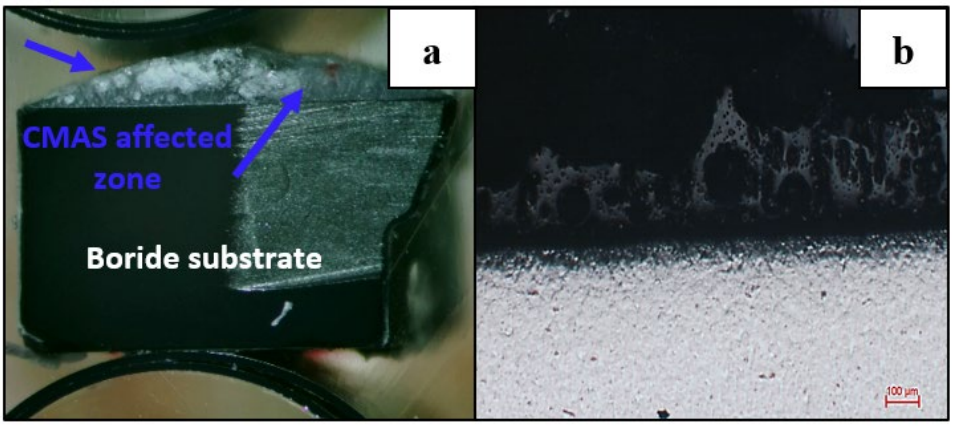

Figure 28. Stereo and optical images of cross sectioned Z3 sample, (a) stereo (b) optical.

Figures 29–31 are the samples exposed to 1300°C for 10 hours. The increase in exposure time resulted in substantially more reaction with the CMAS at the surface. The low magnification optical imagery shows some variation in grain size but does not show substantial infiltration. Like what was observed during the 1 hour test, the B4 sample appears to have the largest reaction with the CMAS experiencing nearly 60% transformation. Table 10 compares the percentage changes after 1 and 10 hours at temperature. The HfB_2 samples seem to perform noticeably better than the other samples with its percent change staying comparatively lower when compared to even the high

percent change of the B3 sample. One feature to note is that the H4 sample displayed the largest difference in percentages between the 1 and 10 hour tests.

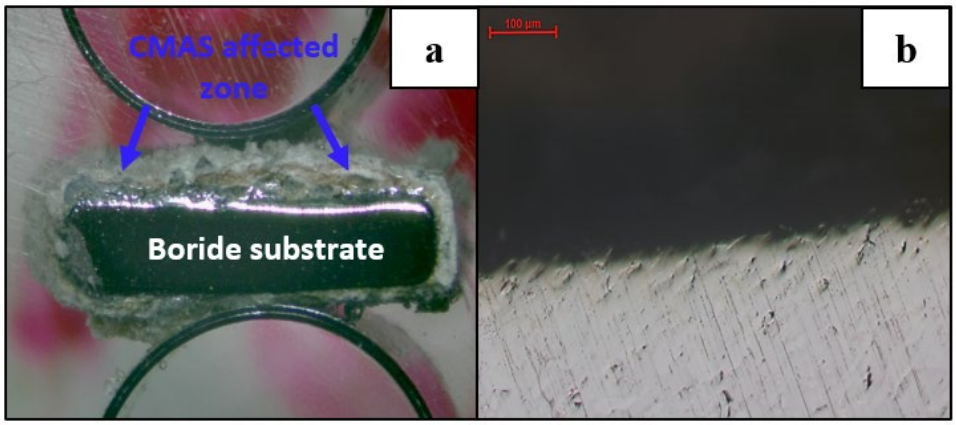

Figure 29. Stereo and optical images of cross sectioned B4 sample, (a) stereo (b) optical.

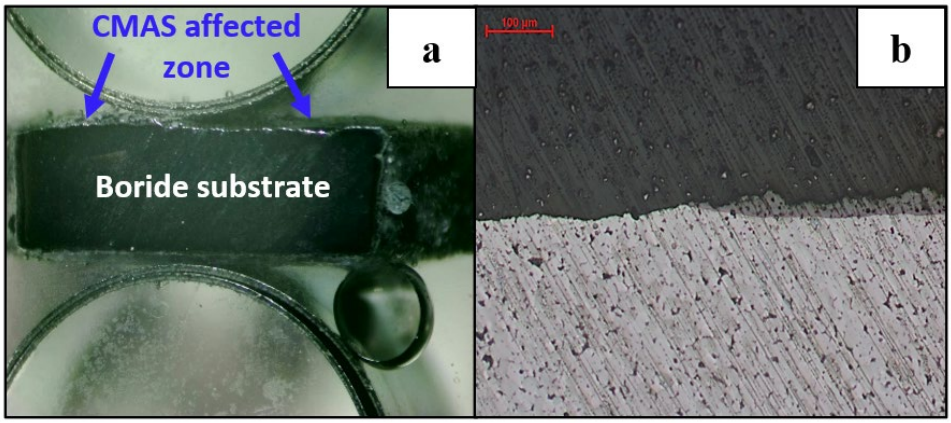

Figure 30. Stereo and optical images of cross sectioned H4 sample, (a) stereo (b) optical.

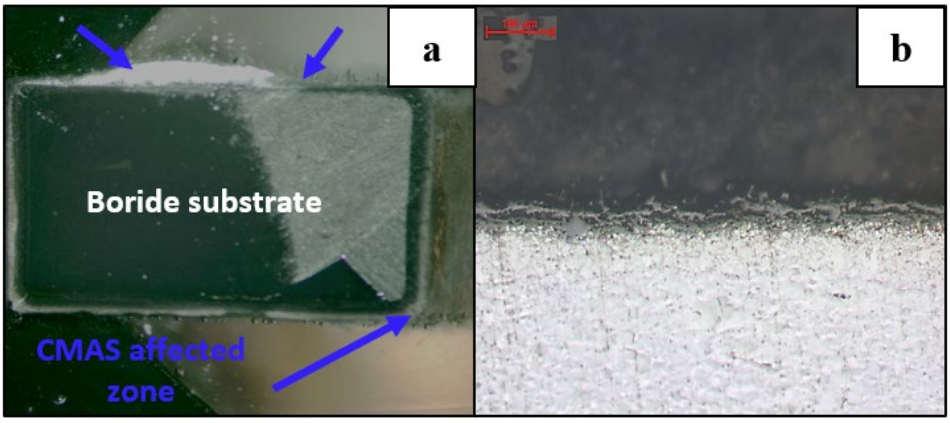

Figure 31. Stereo and optical images of cross sectioned Z4 sample, (a) stereo (b) optical.

Table 10. Approximate percent of material change of samples exposed to 1300°C.

Sample	Percent Change 1 hour	Percent Change 10 hours
HEB	19.58	58.94
HfB_2	5.57	18.44
ZrB_2	16.81	21.01

The 1600°C samples showed significantly more transformation and disintegration than the 1300°C samples. Like the 1300°C tests the HEB samples experienced the most transformation. Based on the low magnification visual inspection, the estimated transformation of the 1 hour sample, B1, was over 50%. This estimate is probably on the low side based on it being calculated from low magnification optical imagery, Figure 32 (b), showing a vastly different structure than the other samples.

The H1 and Z1 samples performed better than the B1 sample. Figures 33 and 34 show that the CMAS infiltrated further into the samples, but the samples maintained a significant amount of the boride substrate. With the H1 and Z1 samples, there are multiple discernable rings around the boride, the inner ring is the transition zone, and the outer is the CMAS glass. Although the transition ring on the H1 is smaller than the Z1 sample, the optical imagery, Figure 33 (b), captures the transition zone nicely. Due to the low

magnification, the grain structure is difficult to discern but the transition zone has less porosity between the grains.

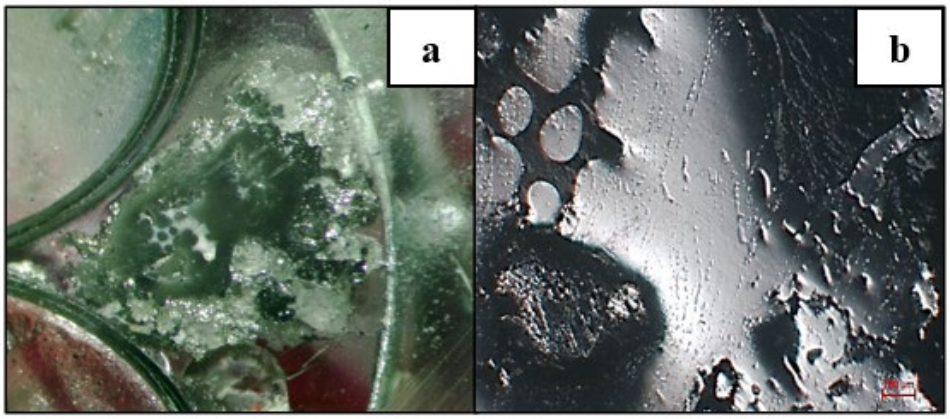

Figure 32. Stereo and optical images of cross sectioned B1 sample, (a) stereo (b) optical.

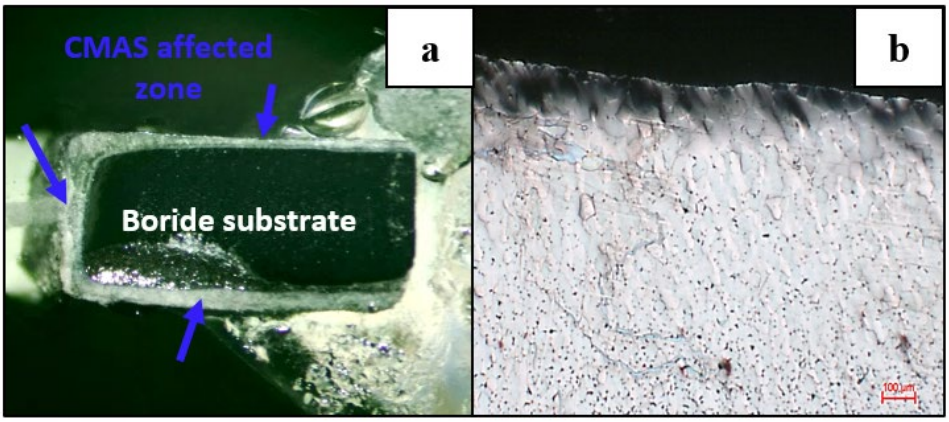

Figure 33. Stereo and optical images of cross sectioned H1 sample, (a) stereo (b) optical.

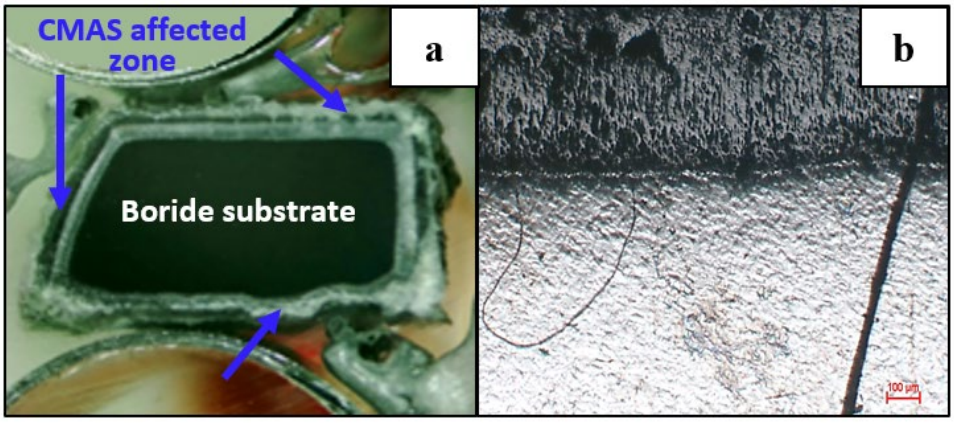

Figure 34. Stereo and optical images of cross sectioned Z1 sample, (a) stereo (b) optical.

Figures 35 and 36 show H2 and Z2 samples exposed to 1600°C for 10 hours. There is no post-test optical imagery of the B2 sample because it experienced total transformation and dissolved through the platinum foil, see Figure 22 (a), so there was nothing left to mount for optical imagery. The H sample still retained some of the original boride material, but the Z2 sample shows indications of total transformation. Figure 35 (b) shows that the H2 maintained its uniform grain structure while Figure 36 (b) shows far less uniformity and greater porosity.

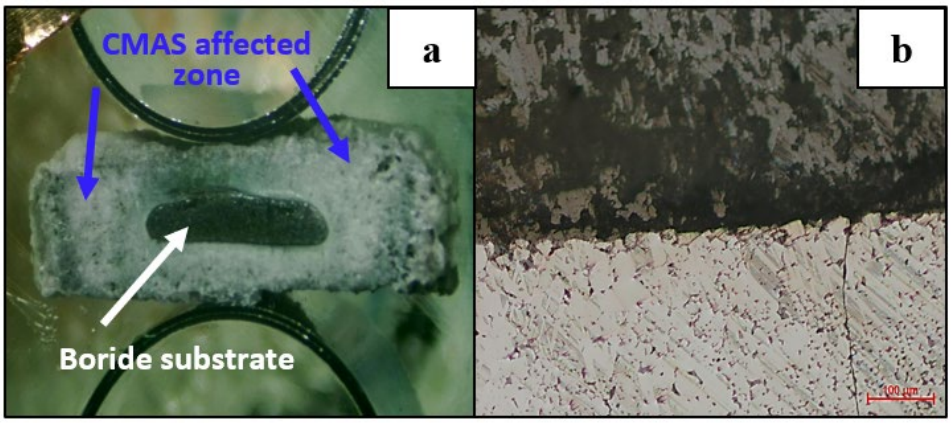

Figure 35. Stereo and optical images of cross sectioned H2 sample, (a) stereo (b) optical.

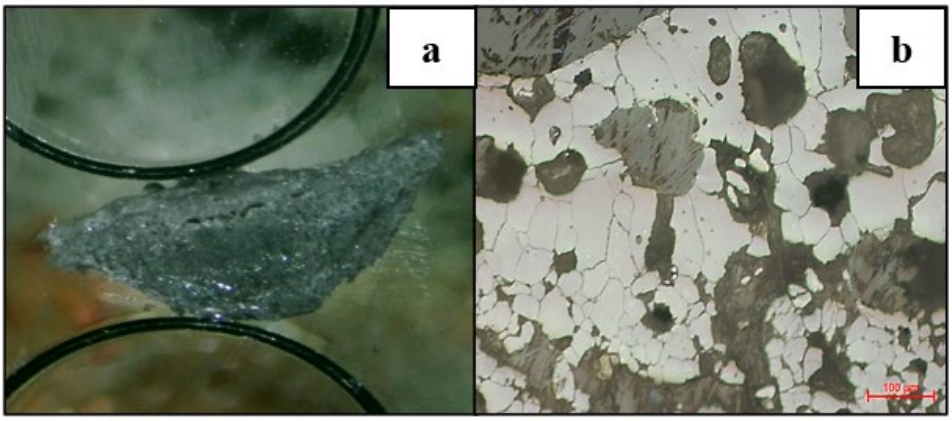

Figure 36. Stereo and optical images of cross sectioned Z2 sample, (a) stereo (b) optical.

Table 11 shows the transformation comparison for the 1600°C samples. For the 1 hour test, the HfB_2 sample experienced about half as much transformation as the HEB sample and about two thirds as much as the ZrB_2 sample. For the 10 hour test, the H2 sample was the only one to not experience total transformation.

Table 11. Approximate percent of material change of samples exposed to 1600°.

Sample	Percent Change 1 hour	Percent Change 10 hours
HEB	58.46	100
HfB_2	26.13	88.80
ZrB_2	41.64	100

C. SCANNING ELECTRON MICROSCOPY

Figures 37–39 shows each of the control samples at 2500x and 5000x magnification. Sample B5, in Figure 37, had the largest initial grain size while sample Z5 had the most refined initial grain size (i.e., fine grain structure). The B5 sample has two types of dark spots throughout, the spots with crisp edges are graphite which was added to the SPS molds to aid in removal. The fuzzier dark spots that lack crisp edges are porosity. The porosity is observed along the grain boundaries while the graphite can be seen both

interstitially and between the grains. This aligns with what Qin et al. observed in their work [41]. The large intergranular cracking observed in sample B5 could be a reason for its poor performance when exposed to CMAS.

The as-received H5 sample, Figure 38, displayed interesting grain structure, the voids between the grains were significantly larger than the other samples but nearly all the voids had smaller particle agglomerations within them. This indicates incomplete densification occurred even though it was reported as experiencing complete densification. The as-received Z5 sample, Figure 39, displayed similar characteristics to the as-received B5 sample with a mix of porosity and graphite dispersed throughout the material.

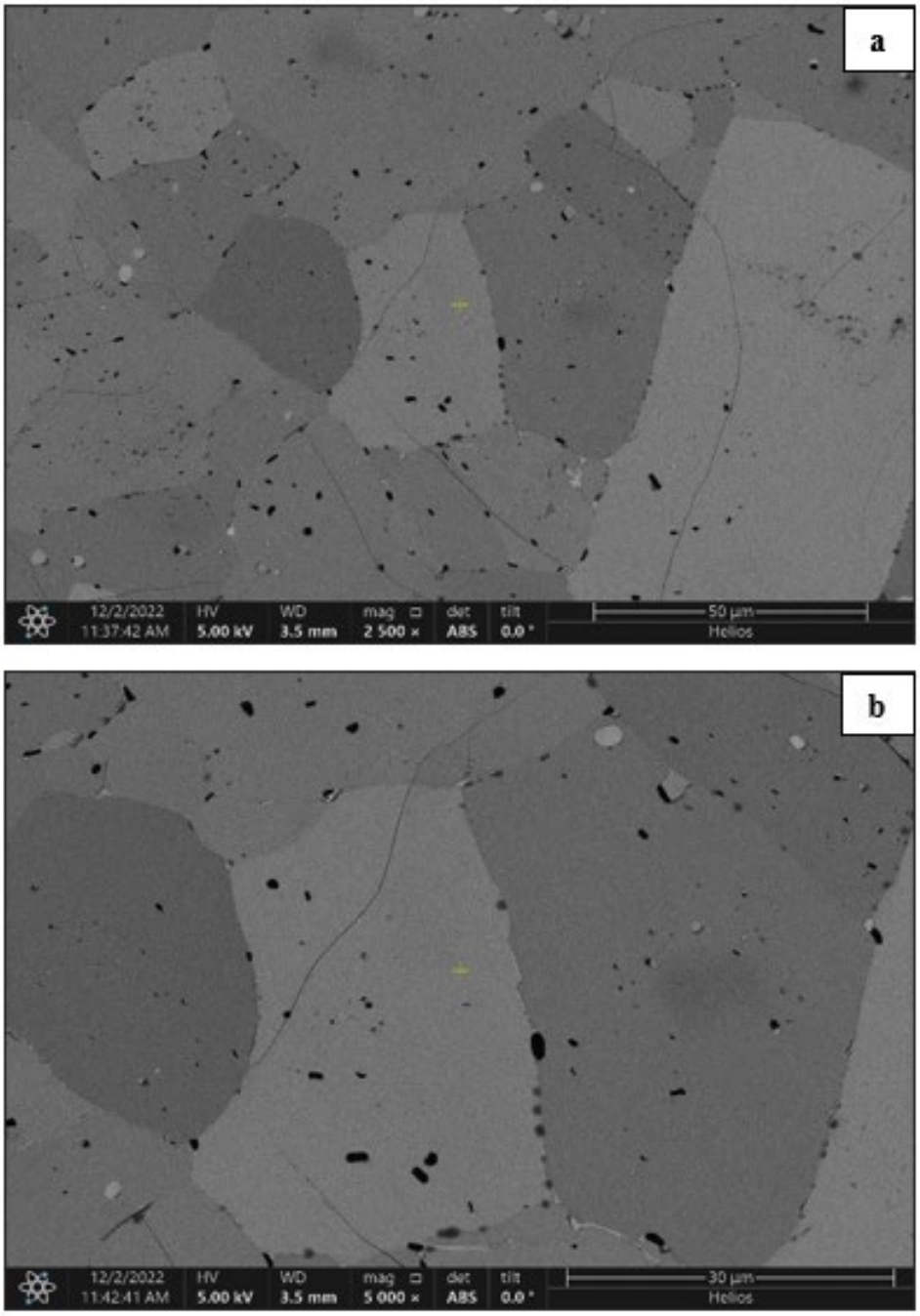

Figure 37. SEM micrographs of HEB control samples, (a) 2500x magnification, (b) 5000x magnification.

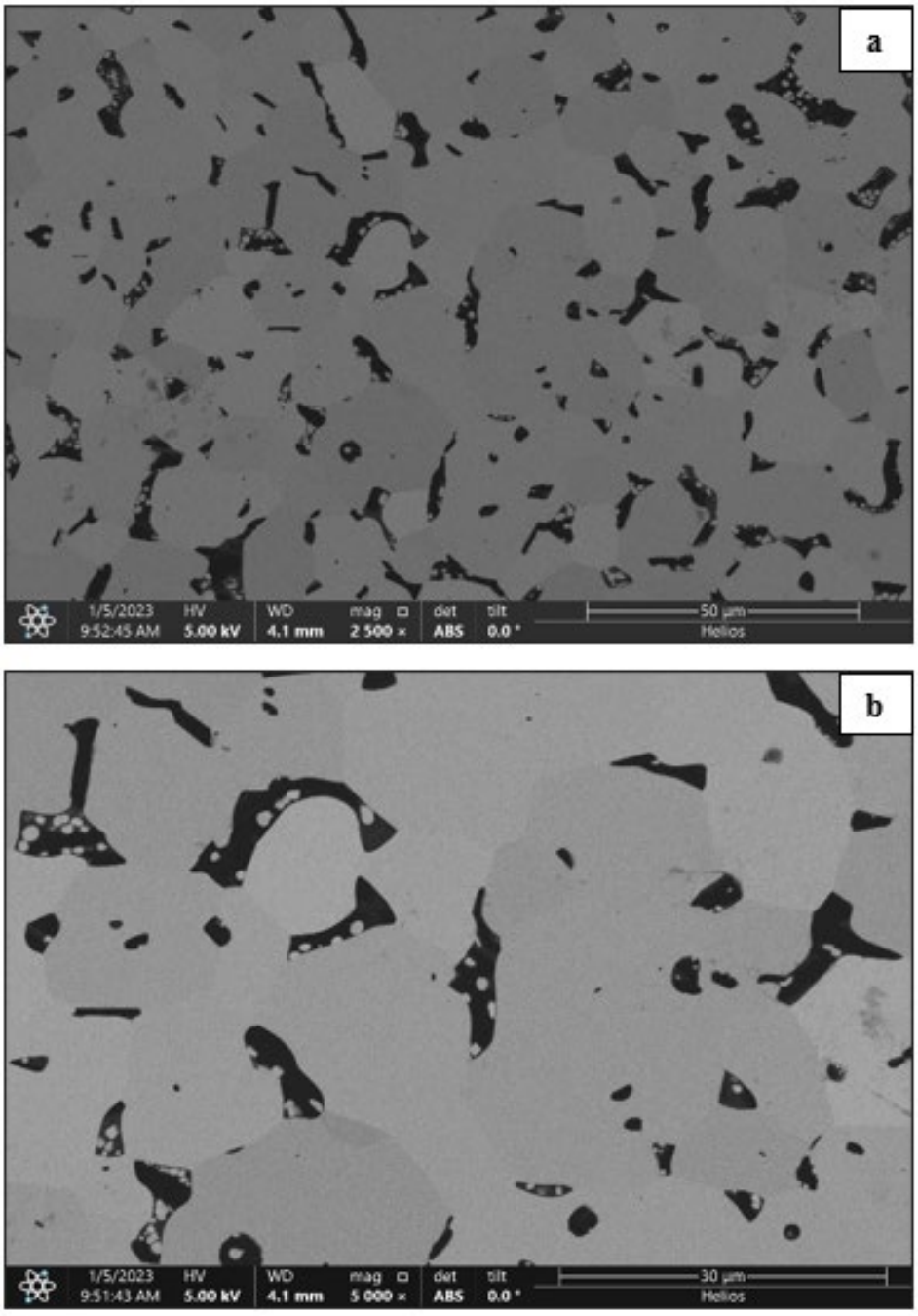

Figure 38. SEM micrographs of HfB_2 control sample, (a) 2500x magnification, (b) 5000x magnification.

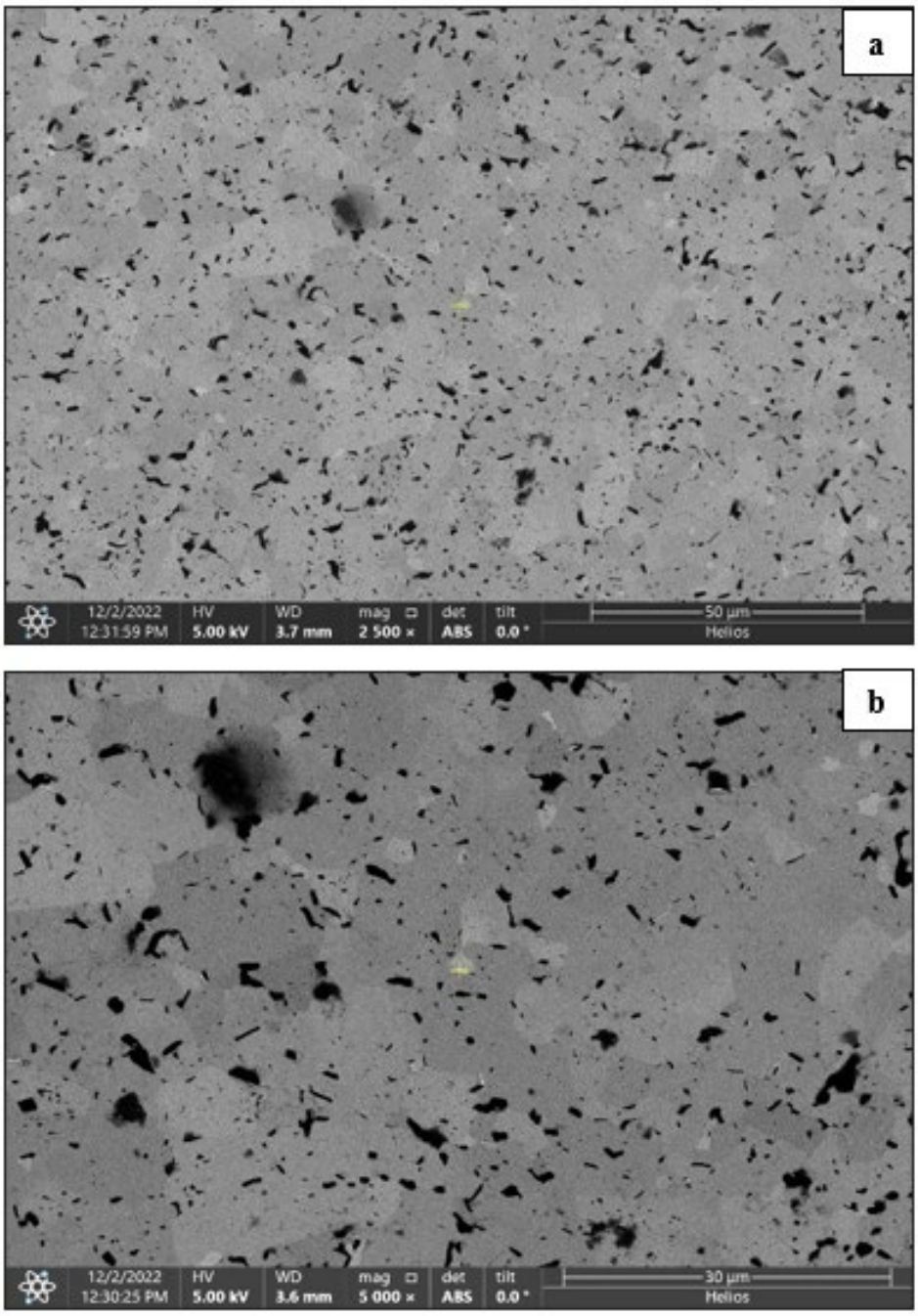

Figure 39. SEM micrographs of ZrB_2 control sample, (a) 2500x magnification, (b) 5000x magnification.

The SEM images of the 1300°C samples exposed for 1 hour are shown in Figures 40–42. In the B3 sample, Figure 40, a significant reduction in grain size was observed along the surface exposed to the CMAS. These small grains are likely oxide particles formed during the reaction between the CMAS and HEB material. At this temperature, the CMAS does not appear to infiltrate into the base material. The small grain size of the oxidation layer resulted in significantly less porosity than what was observed in the base material.

The H3 sample, Figure 41, also formed an oxide layer with grains much smaller than the base material. This hafnia layer has more voids than the oxide layer observed in the B3 sample. The rectangular particles observed between the hafnia layer and the CMAS are likely hafnon, a product of the silicate in CMAS and Hf. The CMAS did not appear to have significant infiltration into the base layer, which appears denser and with fewer voids between grains.

Figure 42 shows that the size of the zirconia (ZrO_2) particles seen in the Z3 sample is comparable to what was observed in the B3 and H3 samples, only appearing larger because the initial grain size is smaller than the other samples. The zirconia layer formed in a more columnar type of structure extending out from the substrate instead of along it like the other samples. Unlike the H3 sample there is no discernible silicon oxide formation.

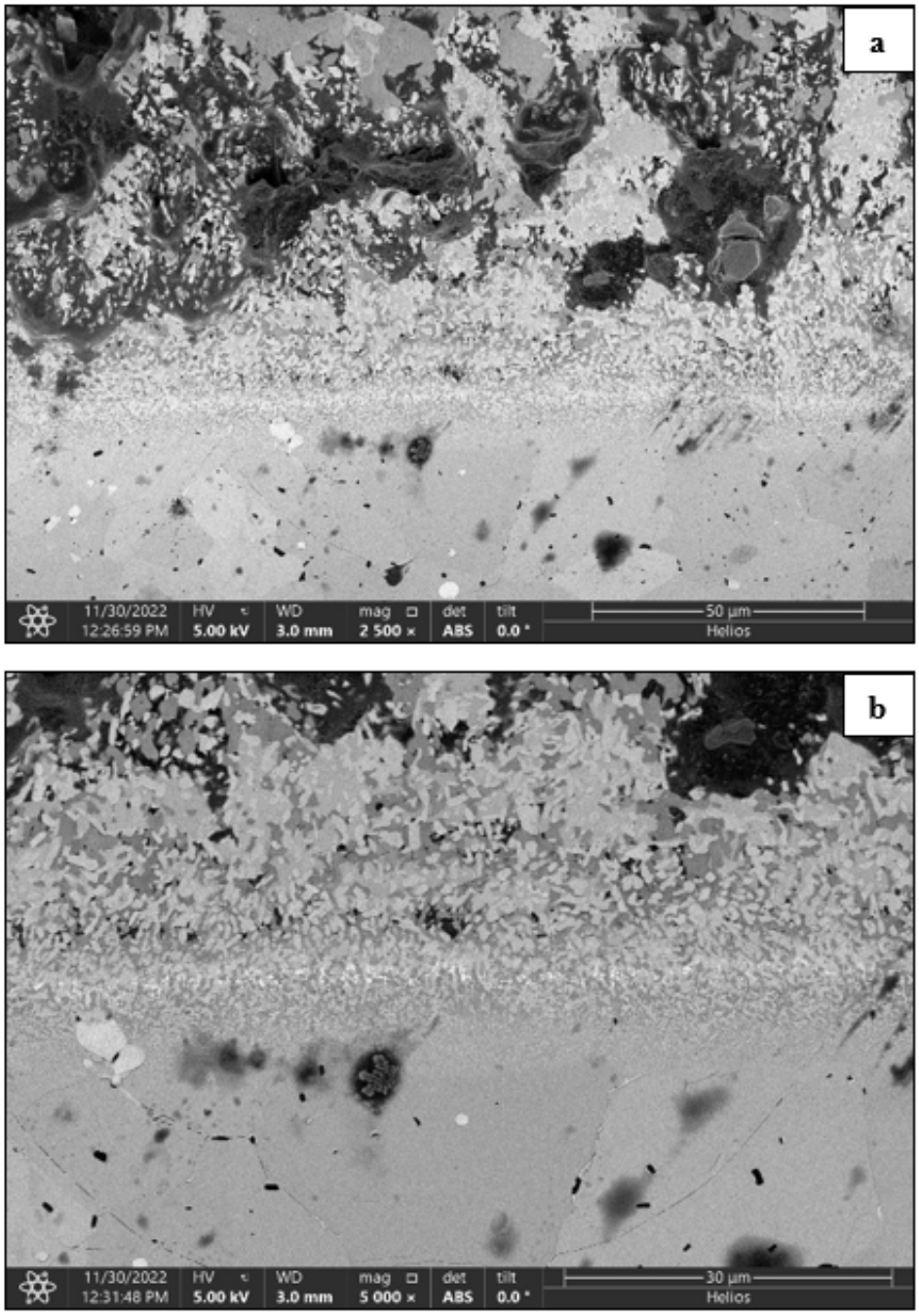

Figure 40. SEM micrographs of HEB exposed to 1300°C for 1 hour, (a) 2500x magnification, (b) 5000x magnification.

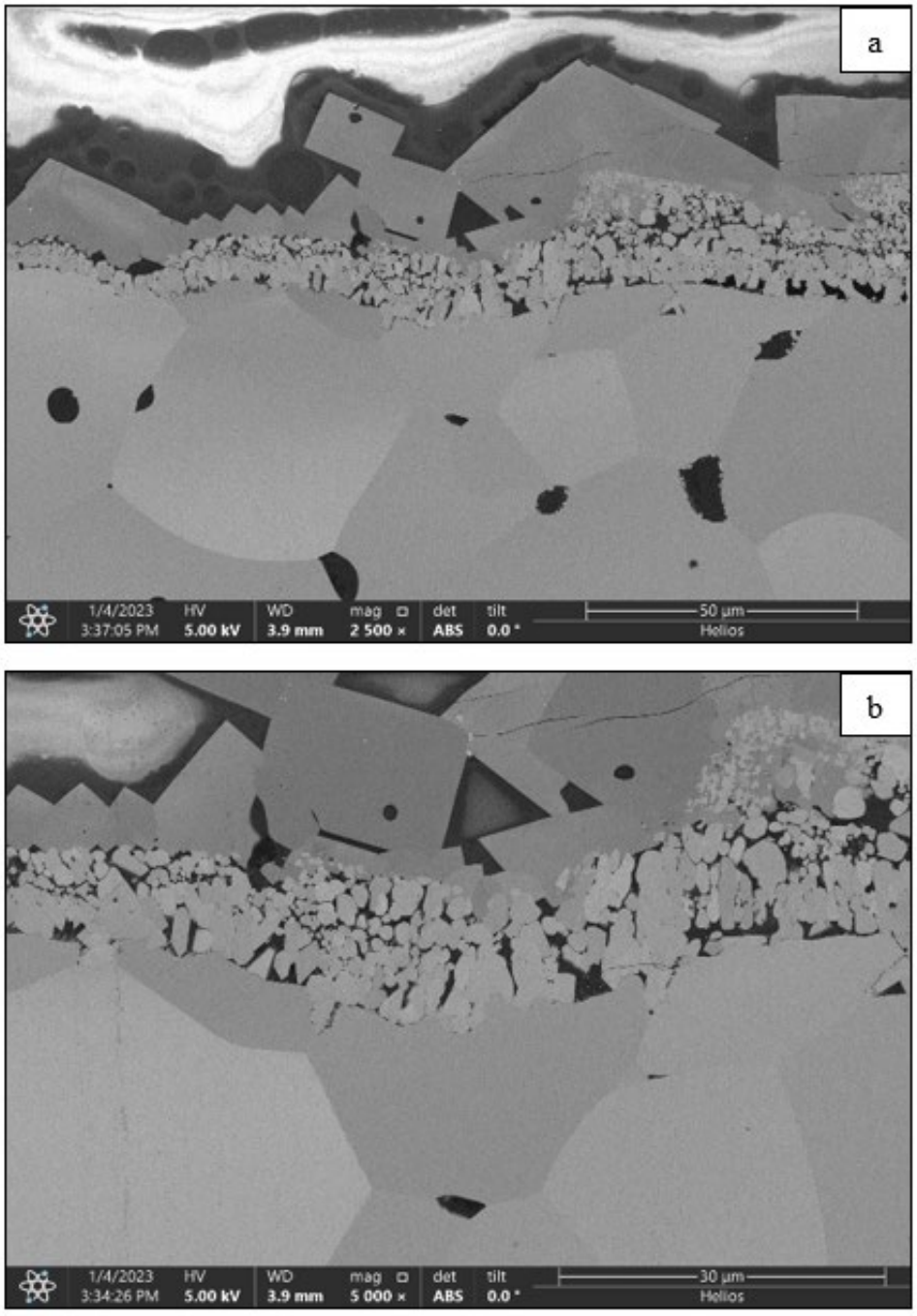

Figure 41. SEM micrographs of HfB_2 exposed to 1300°C for 1 hour, (a) 2500x magnification, (b) 5000x magnification.

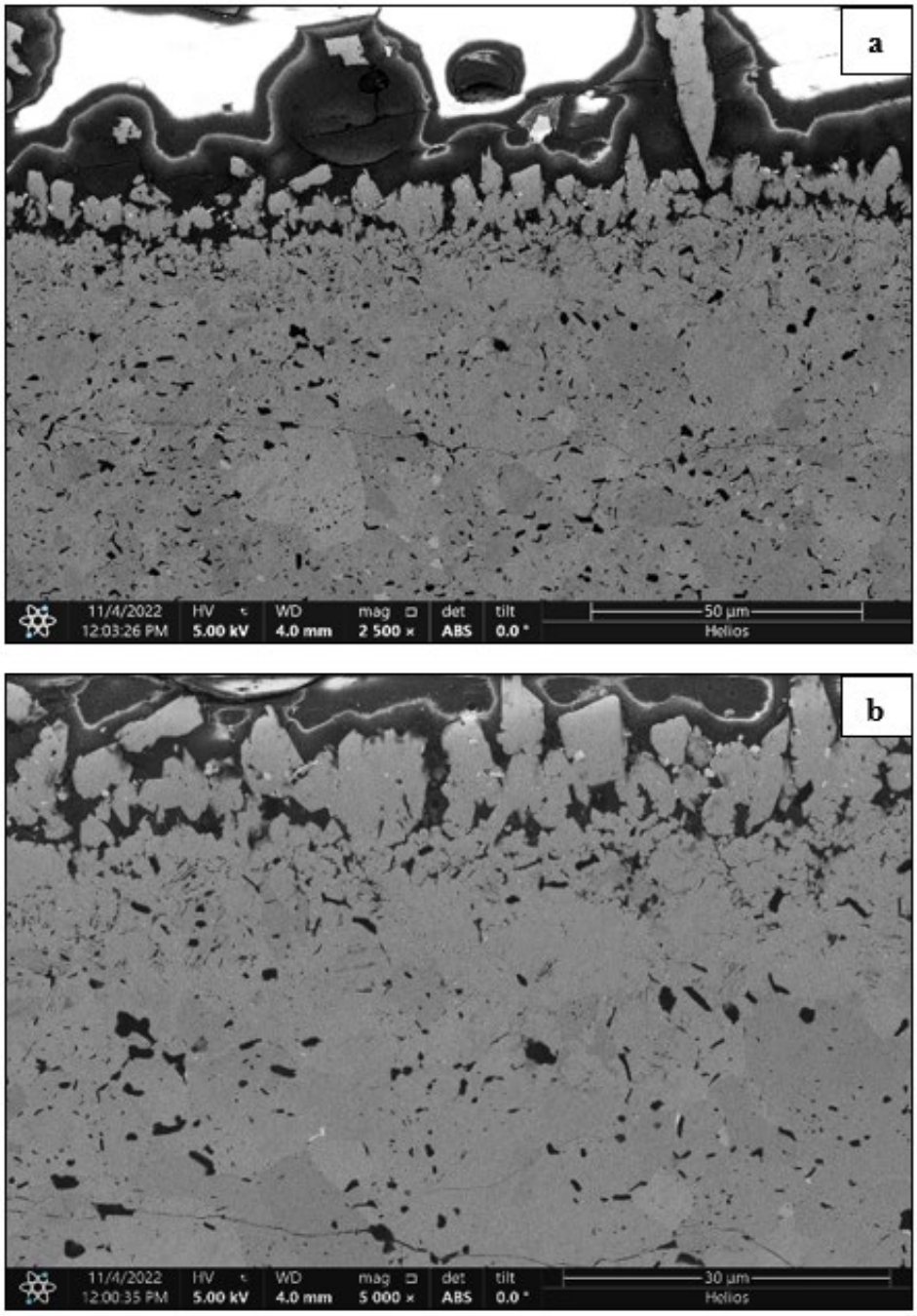

Figure 42. SEM micrographs of ZrB_2 exposed to 1300°C for 1 hour, (a) 2500x magnification, (b) 5000x magnification.

Figures 43–45 are the SEM images of the samples exposed to 1300°C for 10 hours. The oxide layer on the B4 sample, Figure 43, is thicker and more uniform than what was seen in the 1 hour test. This is expected because the increased exposure time means more reaction time. Although it is thicker the grain sizes of the oxide layer appear to be comparable to what was observed in the 1 hour results. One interesting observation is the 10 hour sample has more distinguishable features within the CMAS than the 1 hour test did.

Unlike the 1 hour sample Figure 44 shows no hafnon present in the immediate vicinity of the oxide layer in the 10 hour H4 test. Some densification was observed along the transition layer and the oxide layer forms a more complete film layer than what was observed in the results of the 1 hour test.

Microscopy of the Z4 sample from the 10 hour test, Figure 45, is similar to what was observed in the 1 hour test regarding the growth of the rectangular particles on top of the oxide layer. Based on their shape, these particles show some resemblance to zircon but could not be confirmed due to lack of available chemical analysis instrumentation like an energy dispersive x-ray spectrometer (EDS). The difference being that 10 hour test resulted in larger particles. The oxide layer is more porous than what was observed in the B4 and Z4 samples. This is most likely attributed to the growth of the zircon like particles.

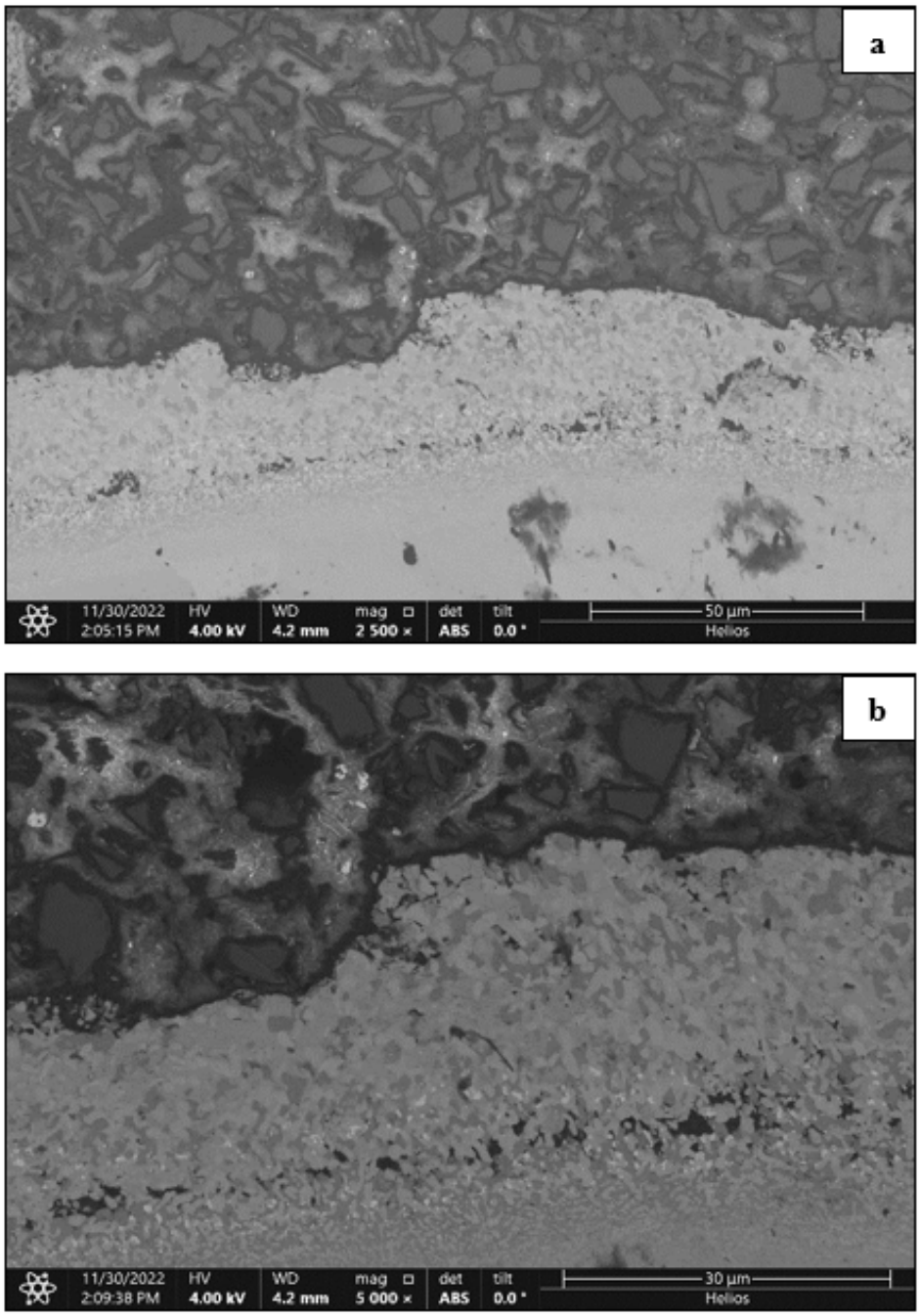

Figure 43. SEM micrographs of HEB exposed to 1300°C for 10 hours, (a) 2500x magnification, (b) 5000x magnification.

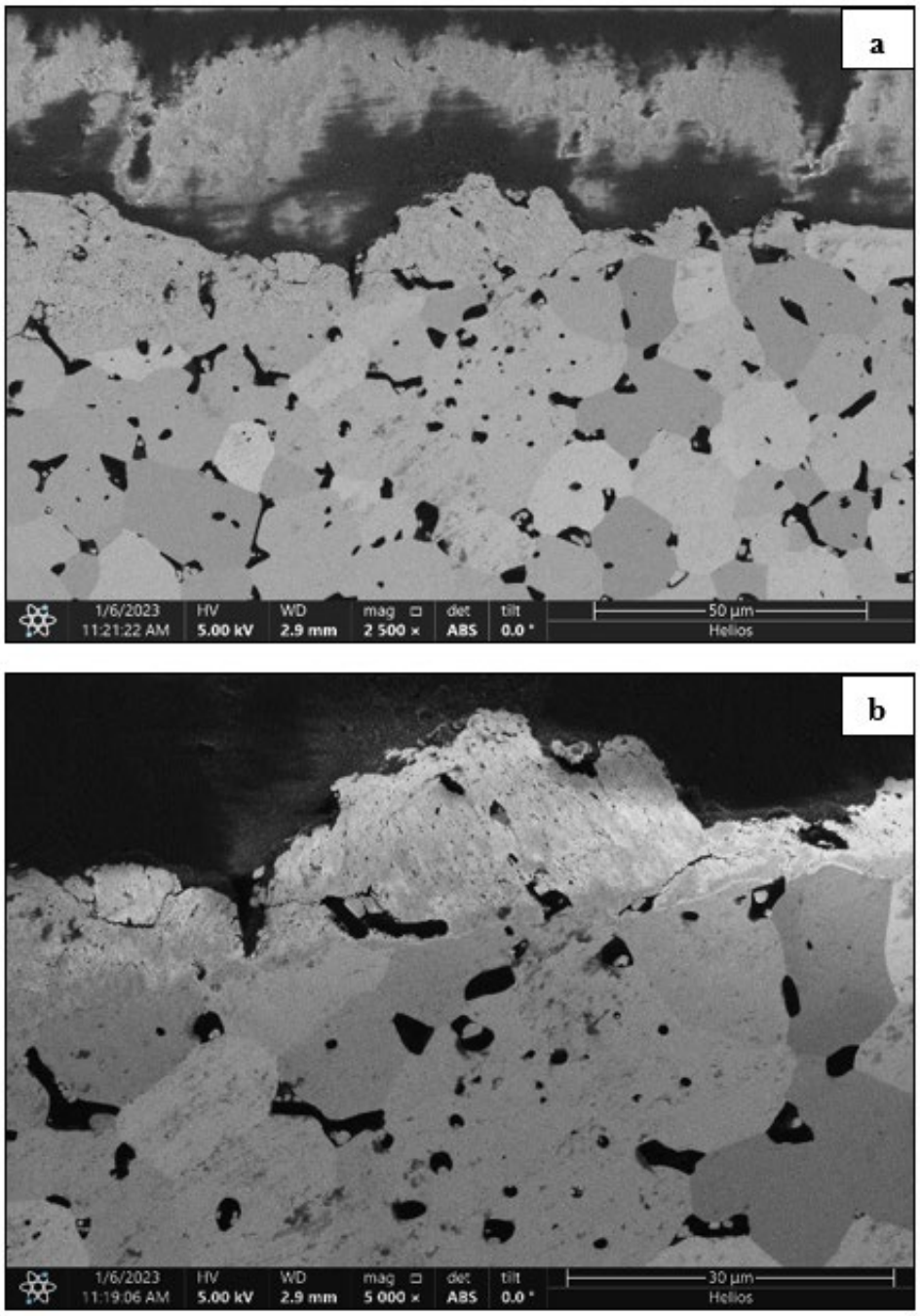

Figure 44. SEM micrographs of HfB_2 exposed to 1300°C for 10 hours, (a) 2500x magnification, (b) 5000x magnification.

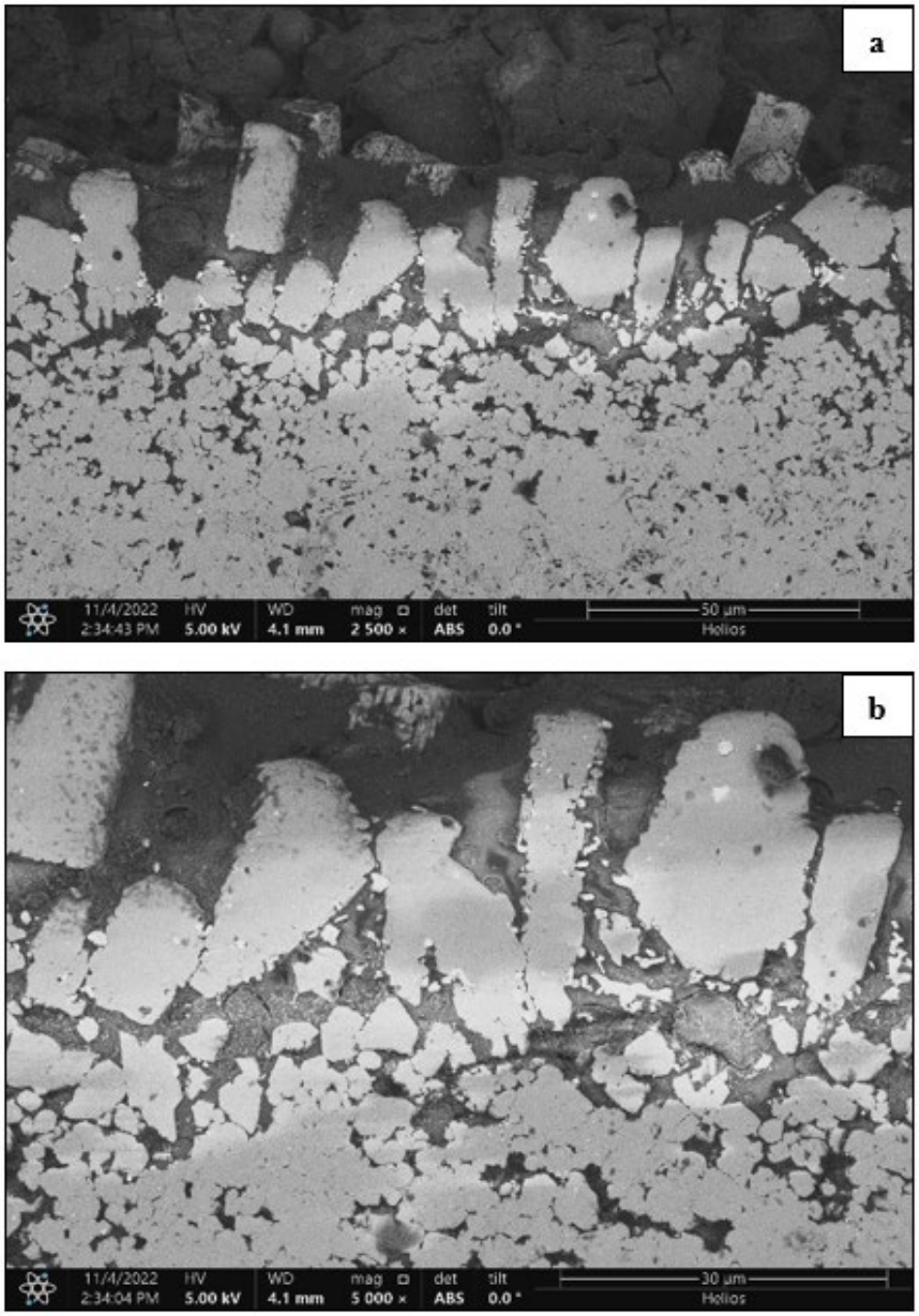

Figure 45. SEM micrographs of ZrB_2 exposed to 1300°C for 10 hours, (a) 2500x magnification, (b) 5000x magnification.

SEM microscopy of the 1600°C samples, Figures 46–51, showed significantly more transformation than the 1300°C samples. On the 1 hour B1 sample, Fig, 46, there are no discernible grains indicating total transformation into an amorphous glass phase. There

is less porosity than what was observed in the control sample but there is an increase in smaller particle inclusions throughout the sample. These inclusions are the lighter gray spots shown in Figure 46.

Unlike the B1 sample, the H1 sample, Figure 47, retained its grain structure with a reduction in intergranular voids near the transition zone. The particles in the oxide layer are more curved and rounded than the rectangular particles observed in the 1300°C samples. In addition to the different shape there are significantly more pores and voids within the particles. This is a result of the boric oxide subliming away from the oxide layer since the exposure temperature is now above its sublimation temperature. With this, a decrease in oxidation resistance would be expected but significant CMAS infiltration was not observed. Additionally, no hafnon was observed at the exposure temperature and time.

Figure 48 is the Z1 sample at this exposure combination which showed more signs of reaction than the H1 sample but not as much as the B1 sample. This can also be observed in the microstructure, at the magnification used in Figure 48 the grain boundaries cannot be easily delineated but the distinct features throughout the sample indicate that it is not amorphous. The region in the vicinity of the CMAS exposure has more dark, amorphous like particles than the adjoining unaffected region. This is believed to be CMAS infiltration because they resemble the particles observed in the darker CMAS region of the image.

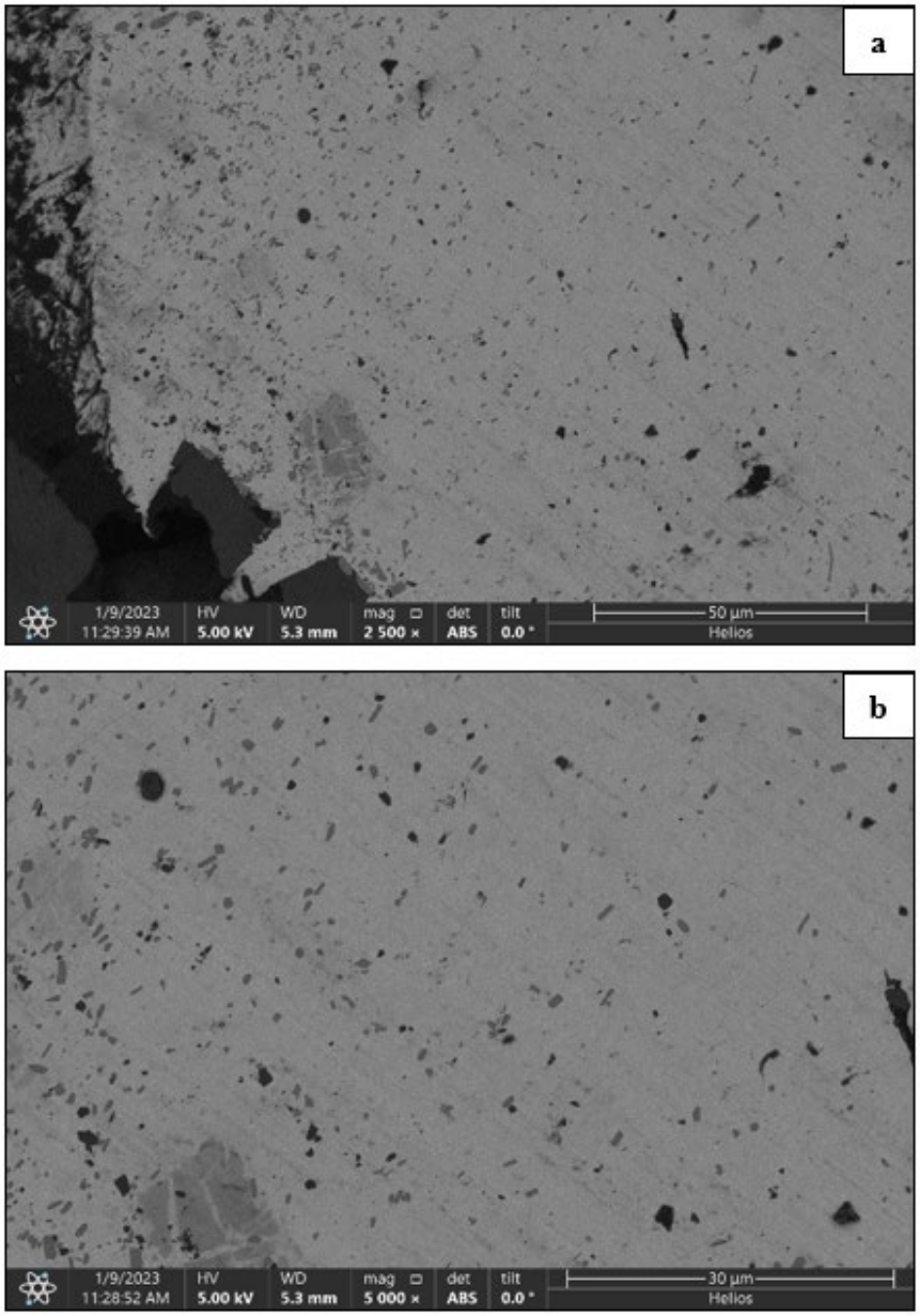

Figure 46. SEM micrographs of HEB exposed to 1600°C for 1 hour, (a) 2500x magnification, (b) 5000x magnification.

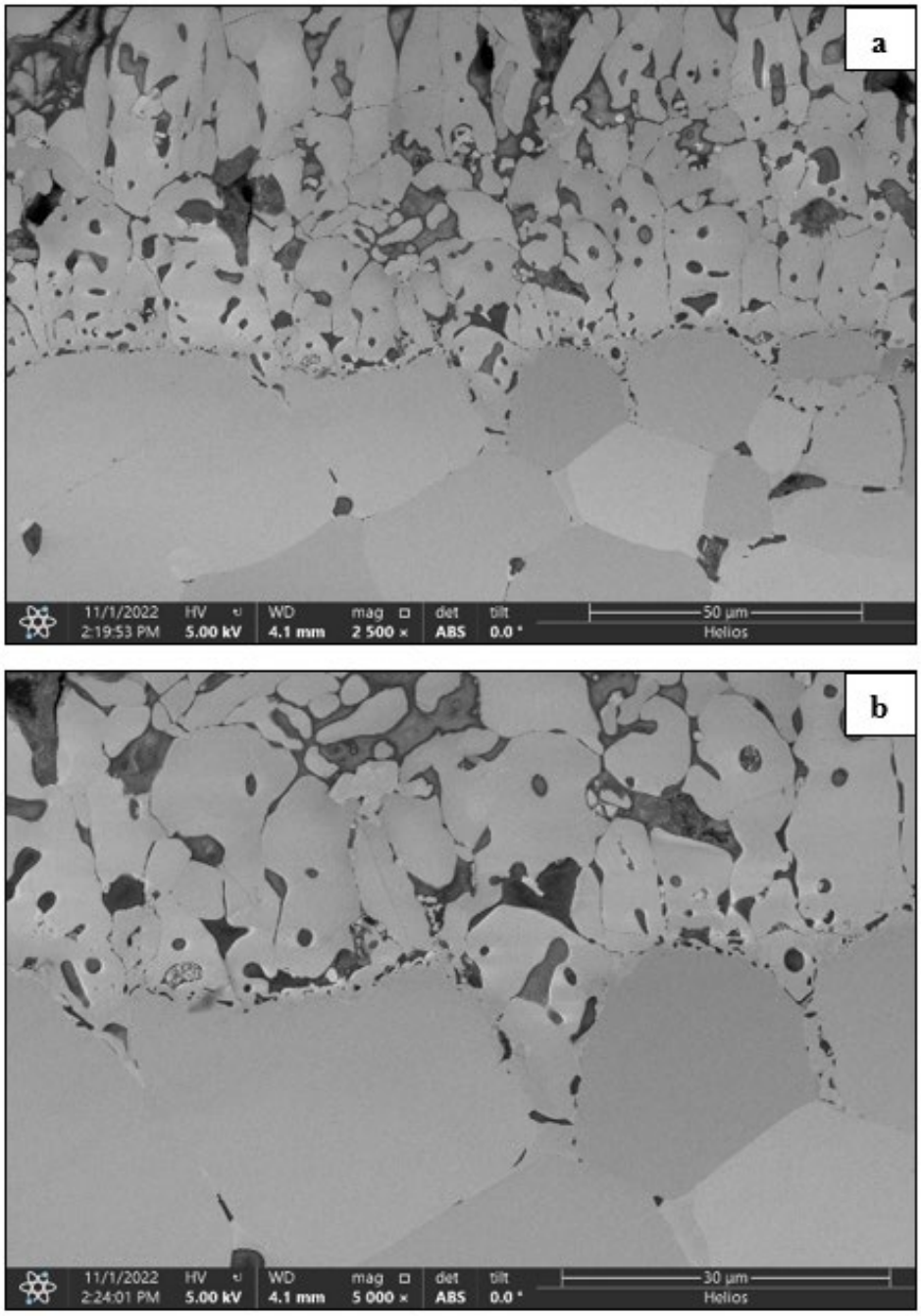

Figure 47. SEM micrographs of HfB_2 exposed to 1600°C for 1 hour, (a) 2500x magnification, (b) 5000x magnification.

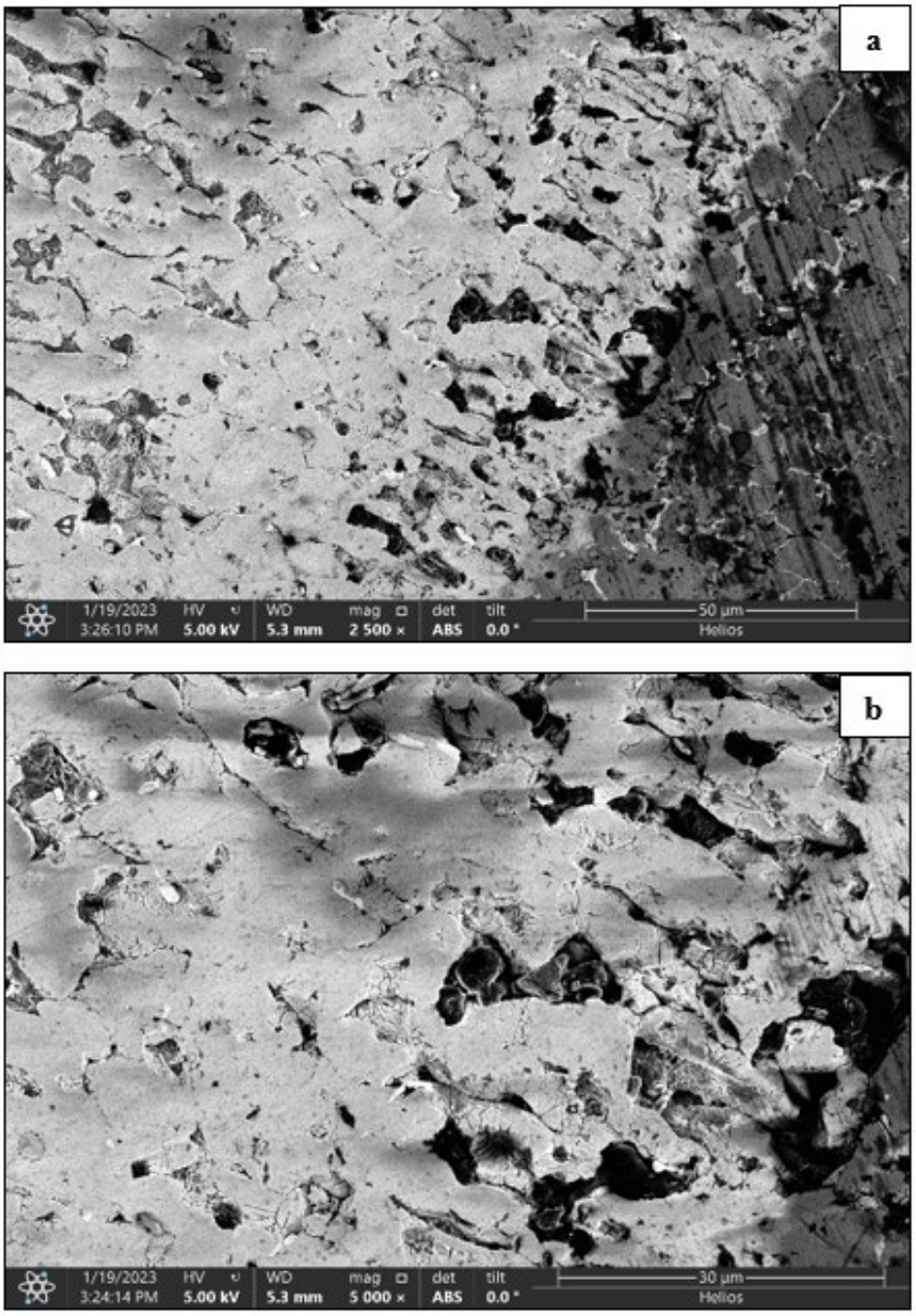

Figure 48. SEM micrographs of ZrB_2 exposed to 1600°C for 1 hour, (a) 2500x magnification, (b) 5000x magnification.

Figures 49–51 show the SEM microscopy of the samples exposed to 1600°C for 10 hours. As discussed previously in this research, sample B2 experienced complete

transformation with no diboride base material remaining. Figure 49 shows that it is completely amorphous having no resemblance to the unexposed control sample.

Even with the increase in exposure time, sample H2, Figure 50, retained its grain structure and did not show signs of significant CMAS infiltration. The grains along the transition and exposure region are slightly more refined and denser than the unaffected region. The densification observed across all the heat treated HfB_2 samples is a likely factor in its superior performance compared to the HEB and ZrB_2 samples. Unlike the 1300°C samples no hafnon was observed along the oxide layer which is also less discernable. The Z2 sample, Figure 51, though not as severe displayed similar transition characteristics to that of the B2 sample at this exposure combination. The Z2 sample experienced significant infiltration which led to an increase in the reaction and material failure.

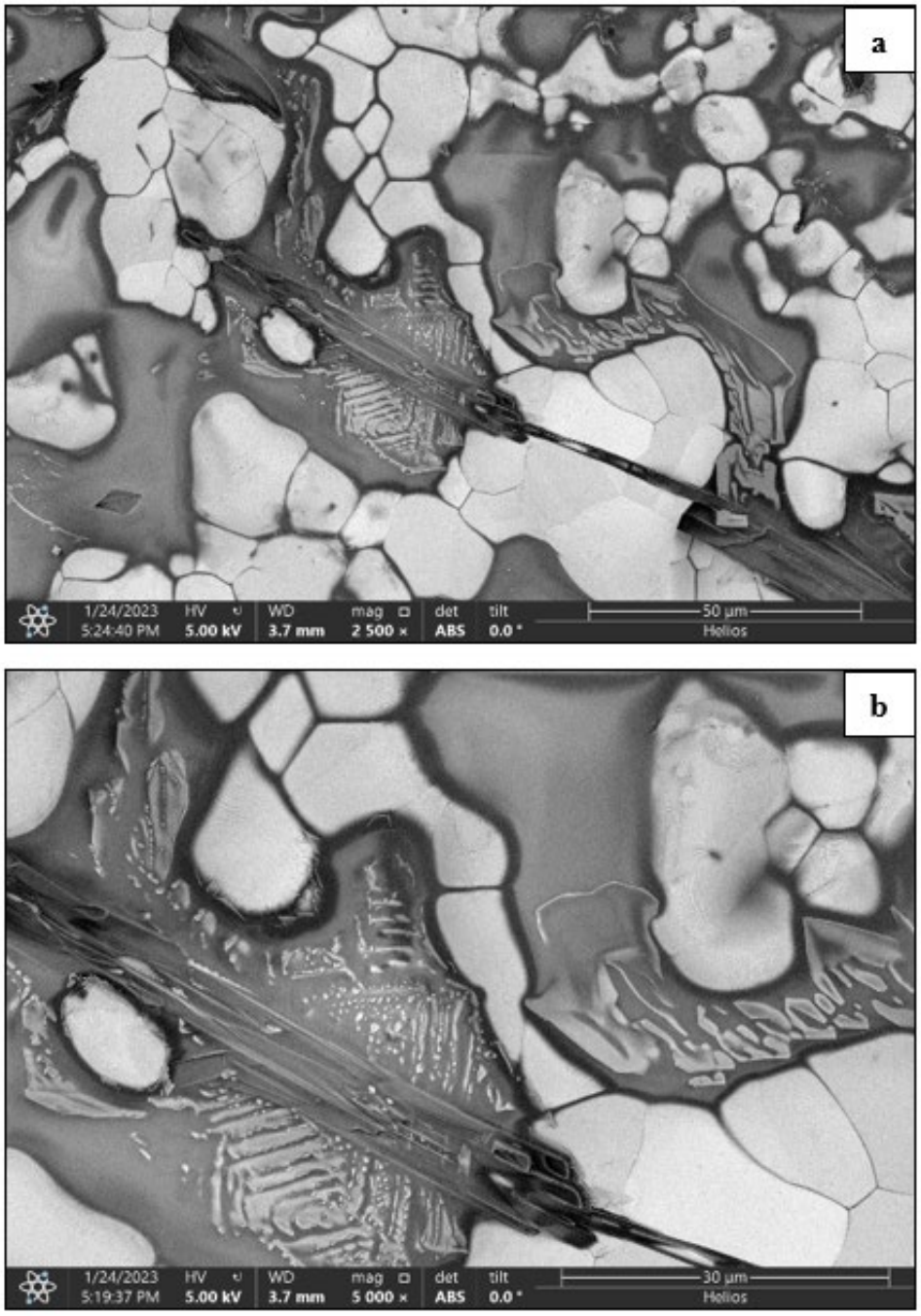

Figure 49. SEM micrographs of HEB exposed to 1600°C for 10 hours, (a) 2500x magnification, (b) 5000x magnification.

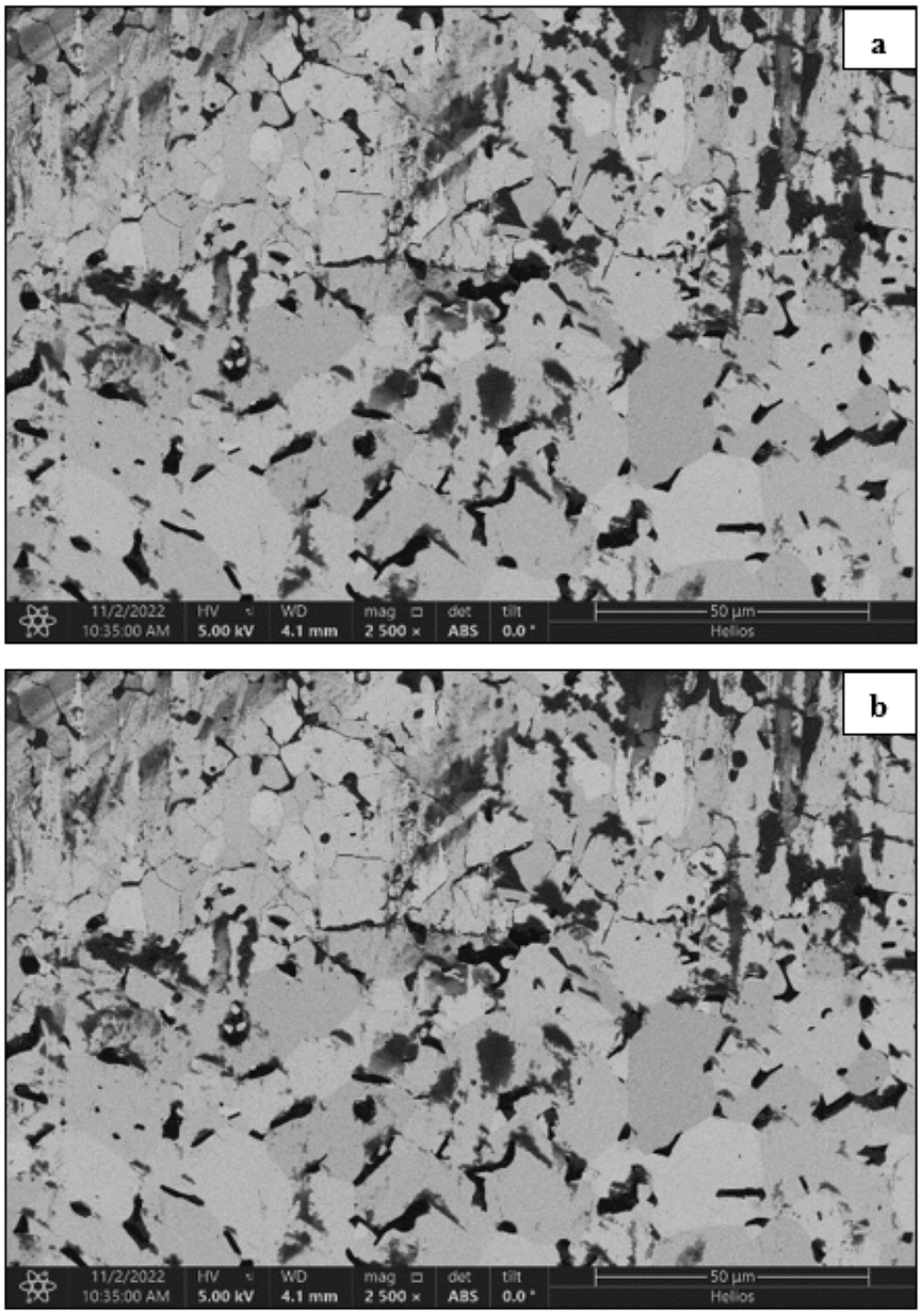

Figure 50. SEM micrographs of HfB_2 exposed to 1600°C for 10 hours, (a) 2500x magnification, (b) 5000x magnification.

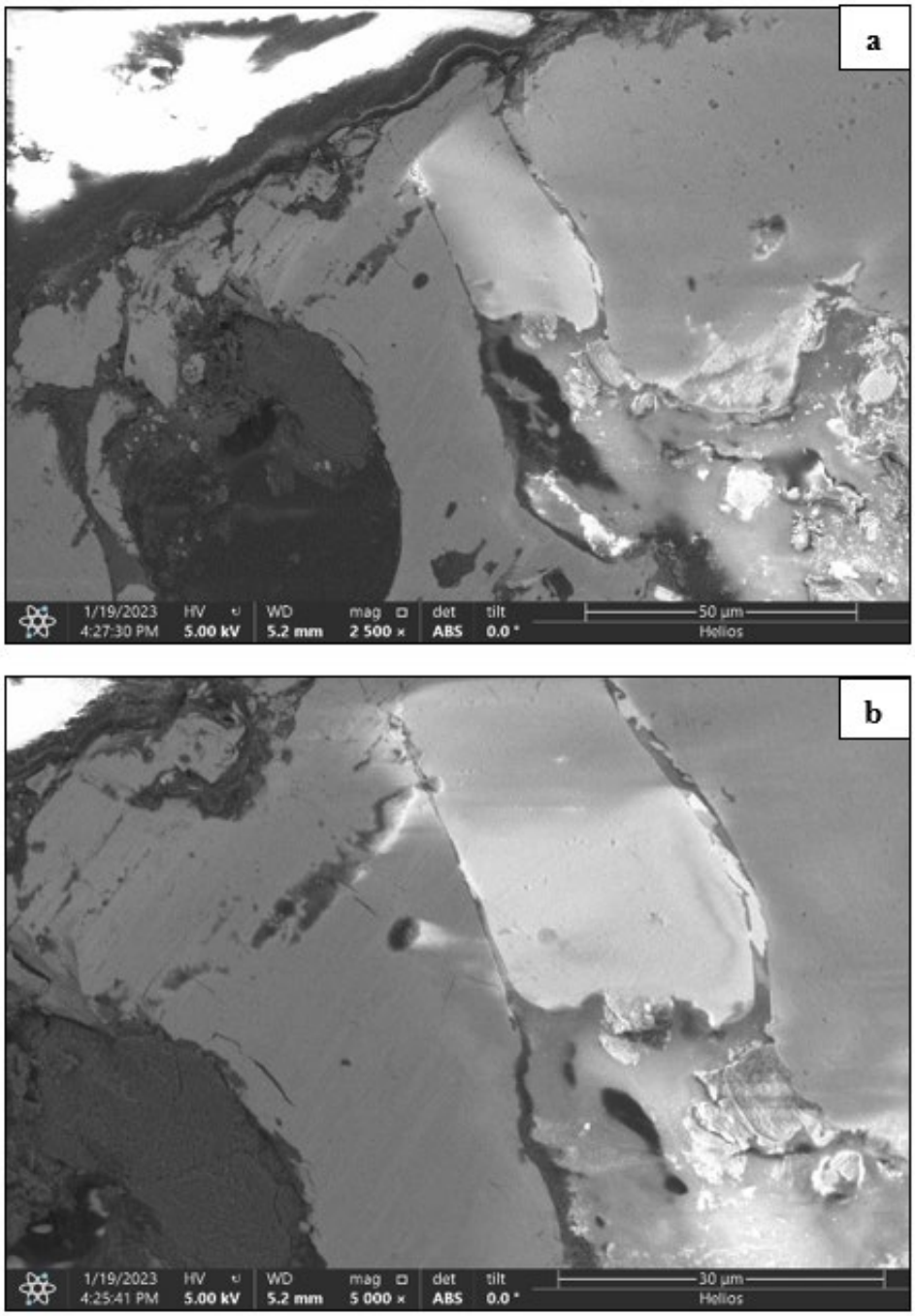

Figure 51. SEM micrographs of ZrB_2 exposed to 1600°C for 10 hours, (a) 2500x magnification, (b) 5000x magnification.

D. X-RAY DIFFRACTION

Since the HEB samples are a newer experimental material, a powder diffraction file (PDF) card could not be located, which made analyzing the crystalline structure and composition challenging. As discussed during the literature review, the HEB used for this testing has an AlB_2 type structure. To analyze the HEB XRD data, the AlB_2 PDF card that most closely aligned with the control sample data was used. This was repeated for the 1300°C for 1 hour sample to determine the Al_2O_3 PDF card with the best fit. These two cards were then used to estimate the compositional percentages of the remaining HEB samples, shown in Table 12. The percentages roughly align with what was observed with stereo and SEM microscopy. There are two sources of potential error in these results, the first one being the lack of specific PDF cards and the second one being the method of grinding the sample to prepare it for XRD analysis. Given the small size and high hardness of the samples there was no way to separate the various layers of the sample before grinding. Thus, the whole sample was ground at one time, likely resulting in considerable mixing between the CMAS, oxide, and substrate layers.

Table 12. HEB sample compositions.

	AlB_2 (%)	**Al_2O_3 (%)**
Control	100	0
1300°C: 1 hour	91.9	8.9
1300°C: 10 hours	15	85
1600°C: 1 hour	-	-
1600°C: 10 hours	-	-
*Calculated using general AlB_2 structure.		

Figure 52 shows combined XRD peak data normalized for all HEB samples. The distinct peaks of the 1300°C samples show that the sample is still crystalline. The large peaks, shown by the dashed lines, are the diboride with the smaller peaks being the oxide, note that the intensity of the oxide increased with the exposure time. The rounded shape of the results at the lower angles of the 1600°C samples indicates that these samples

transitioned to an amorphous phase. The few peaks observed in the 1600°C samples did not correlate to any crystalline peaks.

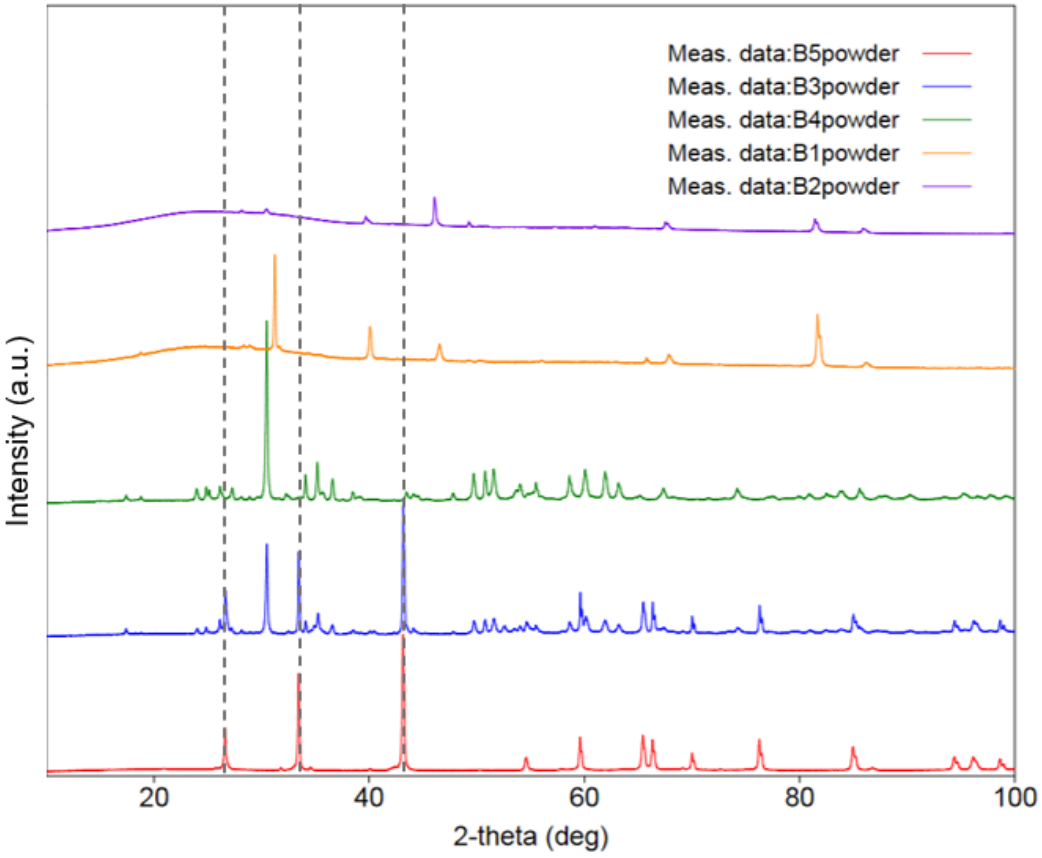

Figure 52. Compiled XRD results of HEB test samples.

Table 13 shows the approximate compositions of the HfB_2 samples. Hafnon was observed in the 1300°C tests but not the 1600°C tests which was expected because the increased temperature caused the boric oxide to evaporate leaving less oxide available to react with the Hf and Si. For the 1300°C test the increase in exposure time resulted in a decrease in hafnon content. This does not align with what was expected and contrary to what Samayoa [5] observed where at 1300°C the presence of hafnon increased with the increase in exposure time. This difference could be attributed to the same mixing of particles while grinding as mentioned in the HEB portion of this section. This is also the probable cause of the apparent increase in HfB_2 seen in the 1300°C samples.

Table 13. HfB_2 sample compositions.

	HfB_2 (%)	**HfO_2 (%)**	**Hafnon (%)**
Control	100	0	0
1300°C: 1 hour	70.8	2.3	26.9
1300°C: 10 hours	82	10	8
1600°C: 1 hour	31.8	68.2	0
1600°C: 10 hours	8.5	91.5	0

The normalized HfB_2 XRD peak data compiled in Figure 53 aligns with what would be expected from sample to sample. The prominent peaks on either side of 40° are the HfB_2, shown by the dashed lines. As the time and temperature increase the smaller oxide peaks become more prevalent. Since the data is normalized the hafnon peaks are not discernible from the oxide peaks.

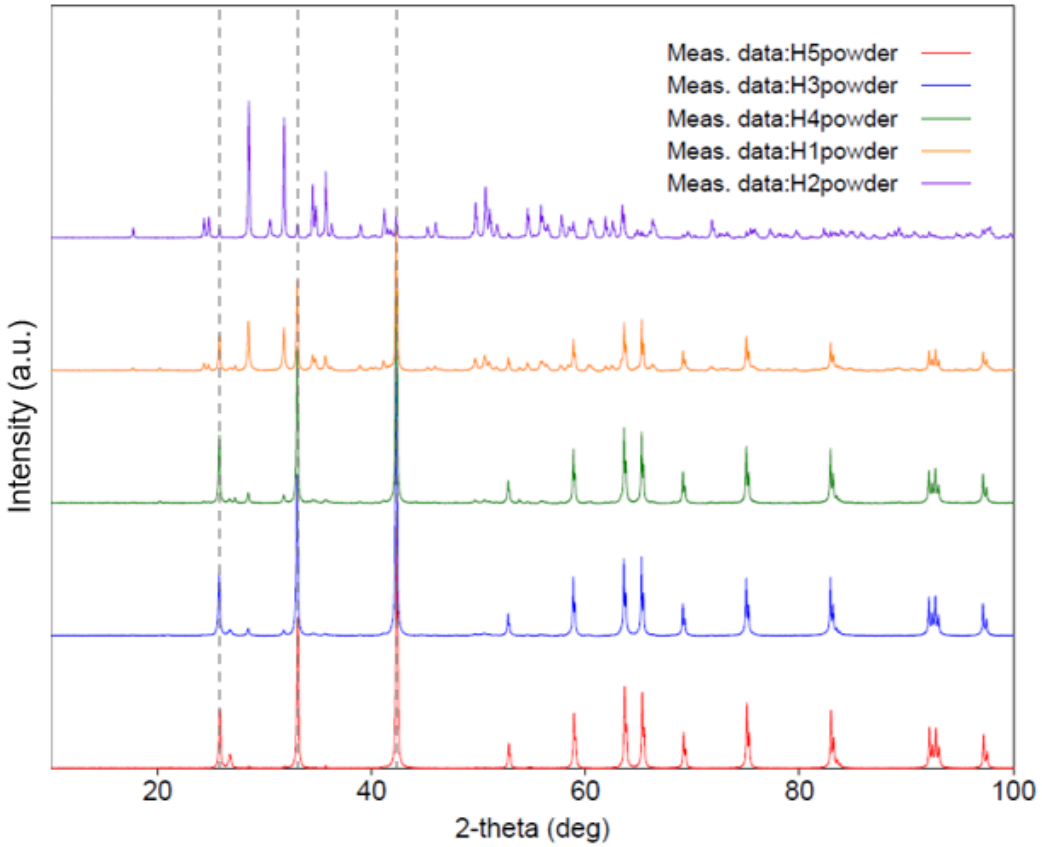

Figure 53. Compiled XRD results of HfB_2 test samples.

The ZrB_2 had similar results, Table 14, to what was observed during the HfB_2 analysis. One key difference is that the silicon oxide compound, zircon, was observed in 1600°C tests. This does not align with what Samayoa [5] observed at 1600°C where there was no trace of zircon present. Like the HfB_2 1300°C tests an increase in boride was observed from the 1 to 10 hour tests which aligns to what was observed with the stereo microscope. As with the other samples this is expected to be a result of the grinding process that was utilized.

Table 14. ZrB_2 sample compositions.

	ZrB_2 (%)	ZrO_2 (%)	Zircon (%)
Control	100	0	0
1300°C: 1 hour	58.4	39.1	2.5
1300°C: 10 hours	77.2	15.75	7.05
1600°C: 1 hour	45.5	52.7	1.8
1600°C: 10 hours	5	88	7

Figure 54 shows the normalized XRD data for ZrB_2. The dashed lines near 40° are ZrB_2, which is observed on all samples except the 10 hours at 1600°C which aligns with the stereo and SEM imagery. The smaller peaks are the oxide which increases with temperature.

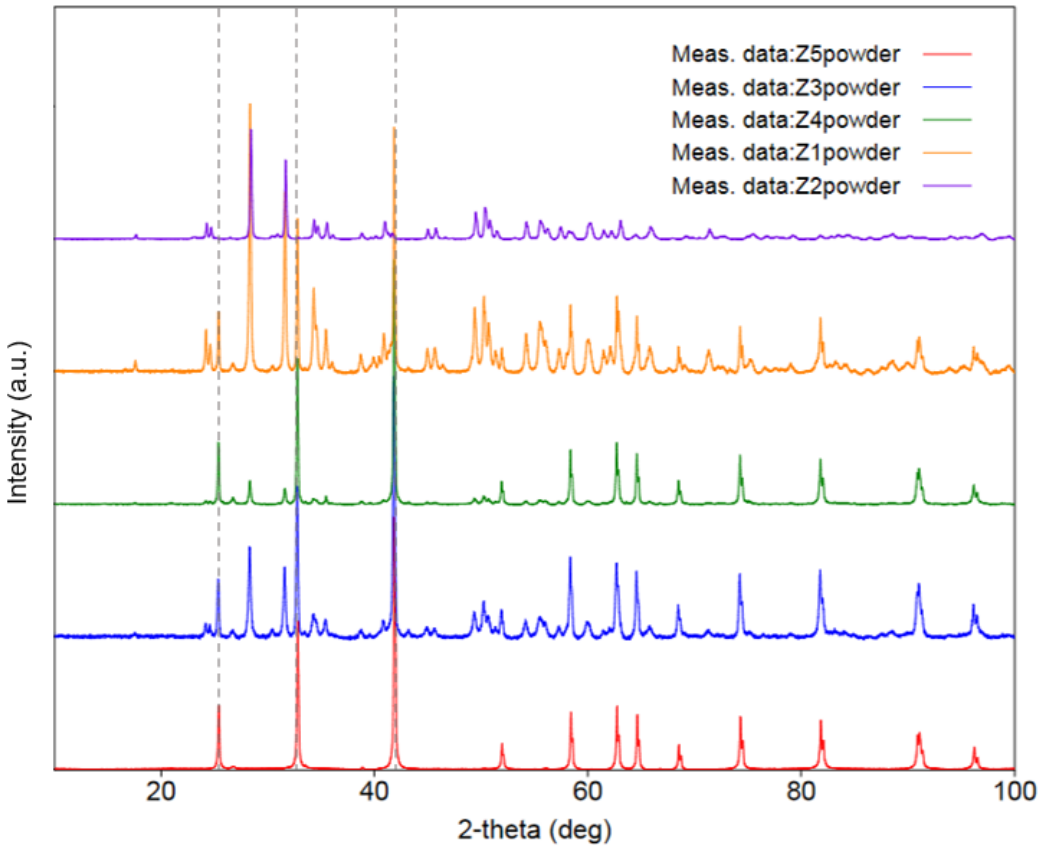

Figure 54. Compiled XRD results of ZrB_2 test samples.

E. NANO-INDENTATION HARDNESS TESTING

Table 15 is the mean modulus and nano hardness for the unexposed control samples. The moduli are significantly lower than what is seen in the available literature, but the hardness aligns with what is published [19], [24], [25], [42]. Based on the SEM images the HEB visually has the largest grain size, but it is significantly harder than the ZrB_2 and HfB_2 samples. This is due to the high amount of elemental substitution in the hexagonal structure caused by the combination of the five elements to achieve the HEB composition [42].

Table 15. Mean modulus and nano hardness of control samples.

Control	Mean Modulus (GPa)	Modulus Std. Dev. (GPa)	Mean Hardness (GPa)	Hardness Std. Dev. (GPa)
HEB	361.16	16.61	35.13	3.48
HfB_2	114.03	8.83	11.11	1.33
ZrB_2	155.51	2.46	14.53	1.09

The nano-indentation hardness results of the samples exposed to 1300°C for 1 hour are shown in Table 16. The HEB showed a general increase in the modulus except for the affected region, which experienced about a 14% decrease. Data from the affected region had a very large standard deviation, which can explain why a decrease was observed. The affected region was the only region to show a significant decrease in hardness with a reduction of nearly 50%.

The HfB_2 and ZrB_2 had different results than the HEB but displayed similar performance to one another. Both samples experienced a significant increase in their modulus regardless of location within the sample. An increase in hardness was also observed with the HfB_2 more than doubling in hardness compared to the control sample. For all three samples the hardest region of the sample was the transition region which was likely due to hardness of the oxides formed in that region.

Table 16. Mean modulus and nano hardness: 1300°C for 1 hour.

1300°C: 1 hour	Mean Modulus (GPa)	Modulus Std. Dev. (GPa)	Mean Hardness (GPa)	Hardness Std. Dev. (GPa)
HEB (affected)	310.41	87.05	18.81	9.65
HEB (transition)	437.74	16.37	35.66	3.97
HEB (unaffected)	397.87	27.96	31.15	2.41
HfB_2 (affected)	496.54	13.40	29.96	3.24
HfB_2 (transition)	505.76	12.34	29.89	0.72
HfB_2 (unaffected)	385.01	30.43	19.46	2.92
ZrB_2 (affected)	365.02	27.01	20.07	3.50
ZrB_2 (transition)	368.26	17.99	19.63	2.07
ZrB_2 (unaffected)	394.70	18.21	19.78	1.45

Table 17 shows the nano-indentation results of the samples exposed to 1300°C for 10 hours. The modulus performance of the HEB exposed to 1300°C for 10 hours was contrary to what was observed in the 1 hour results with the HEB's modulus decreasing by more than 60%. The HEB had considerable variation between the regions as well. The HfB_2 modulus showed only a slight increase compared to the substantial increase observed in the 1 hour test. The ZrB_2 modulus increased by approximately the same as it did during the 1 hour test. The HEB and HfB_2 both experienced a decrease in their hardness while ZrB_2 hardness increased by an average of 27%.

Table 17. Mean modulus and nano hardness: 1300°C for 10 hours.

1300°C: 10 hours	Mean Modulus (GPa)	Modulus Std. Dev. (GPa)	Mean Hardness (GPa)	Hardness Std. Dev. (GPa)
HEB (affected)	239.77	29.44	20.16	4.13
HEB (transition)	112.06	20.33	8.69	2.31
HEB (unaffected)	67.12	13.92	4.98	1.65
HfB_2 (affected)	125.59	26.80	7.15	2.02
HfB_2 (transition)	146.19	22.05	9.03	1.48
HfB_2 (unaffected)	156.71	29.34	11.32	3.79
ZrB_2 (affected)	384.34	16.40	20.63	1.69
ZrB_2 (transition)	365.27	45.49	19.14	4.07
ZrB_2 (unaffected)	392.84	16.79	20.75	2.13

The nano-indentation hardness results of the samples exposed to 1600°C for 1 hour are shown in Table 18. The HEB experiences a substantial decrease in both modulus and hardness which is due to the near total transformation observed. The HfB_2 and ZrB_2 experienced an increase in both modulus and hardness. The moduli of both samples are still below the published values discussed earlier in this report but are much closer, the HfB_2 is within 18% and the ZrB_2 is within 30%. The hardness results are comparable to what was observed in the 1300°C test where the HfB_2 value is more than double that of the control sample and the ZrB_2 is slightly harder than the control sample.

Table 18. Mean modulus and nano hardness: 1600°C for 1 hour.

1600°C: 1 hour	Mean Modulus (GPa)	Modulus Std. Dev. (GPa)	Mean Hardness (GPa)	Hardness Std. Dev. (GPa)
HEB (affected)	77.76	37.46	1.46	0.29
HEB (transition)	-	-	-	-
HEB (unaffected)	-	-	-	-
HfB_2 (affected)	385.60	37.17	25.71	3.98
HfB_2 (transition)	400.49	18.86	29.16	1.40
HfB_2 (unaffected)	397.54	21.59	28.93	3.77
ZrB_2 (affected)	314.18	29.58	15.56	3.57
ZrB_2 (transition)	358.05	10.13	17.56	1.32
ZrB_2 (unaffected)	363.19	14.70	16.75	1.10

The nano-indentation hardness results of the samples exposed to 1600°C for 10 hours are shown in Table 16. Nano testing was not performed on the HEB because there was no sample remaining to test. The modulus of the HfB_2 decreased in the affected region and increased in the transition and unaffected region. The high standard deviations of these tests indicate that there is significant error in these results. The hardness also decreased in the affected region while increasing in the transition and unaffected regions. ZrB_2 also experienced near total transformation and thus was only able to be tested in the affected region. The substantial decrease in both modulus and hardness further supports that the sample experienced total transformation and no ZrB_2 remained.

Table 19. Mean modulus and nano hardness: 1600°C for 10 hours.

1600°C: 10 hours	Mean Modulus (GPa)	Modulus Std. Dev. (GPa)	Mean Hardness (GPa)	Hardness Std. Dev. (GPa)
HEB (affected)	-	-	-	-
HEB (transition)	-	-	-	-
HEB (unaffected)	-	-	-	-
HfB_2 (affected)	87.02	26.81	3.37	2.23
HfB_2 (transition)	355.02	70.30	19.06	7.09
HfB_2 (unaffected)	366.06	77.08	17.87	7.45
ZrB_2 (affected)	27.45	12.49	0.33	0.30
ZrB_2 (transition)	-	-	-	-
ZrB_2 (unaffected)	-	-	-	-

V. CONCLUSION

A. SUMMARY

Samples of a high entropy boride and two metal diborides, HfB_2 and ZrB_2, all prepared via spark plasma sintering, performed reasonably well against CMAS attack at 1300°C. The performance of these ceramics varied greatly at 1600°C. Although the HEB is observed to have impressive physical and mechanical properties at elevated temperatures, it performed the worst of the three materials tested. Even at the lower exposure time it experienced significantly more transformation and softening than the HfB_2 and ZrB_2 samples. All the samples experienced oxidation which is a result of atmospheric oxygen and substrate interacting at elevated temperatures. However, the HfB_2 and ZrB_2 tested at 1300°C were the most oxidized by the CMAS, determined by the likely presence of hafnon (in HfB_2) and zircon (in ZrB_2). The samples exposed to longer durations and higher temperatures showed a decrease in silicon oxide content. This indicates that both samples have potential as materials for next-generation GTE applications, with HfB_2 being more favorable than ZrB_2. Future research is needed to reduce oxidation of the borides at elevated temperatures, but these materials are a step in the right direction in achieving improved engine life and lowering maintenance and upkeep costs of GTEs.

B. FUTURE WORK

Further analysis is needed to obtain a more complete understanding of the performance of HEB, HfB_2, and ZrB_2 when exposed to CMAS. Future work includes EDS/ EBSD analysis of samples to determine the actual amount of infiltration and transformation. Thermogravimetric analysis and differential scanning calorimetry should also be performed to evaluate the rate and degree of reaction. Additionally, evaluation of the glass transition points of CMAS glass should be studied, in particular how to promote an earlier transition to reduce the amount of oxidation occurring with the boride substrates.

THIS PAGE INTENTIONALLY LEFT BLANK

LIST OF REFERENCES

[1] M. J. Walock, V. Heng, A. Nieto, A. Ghoshal, M. Murugan, and D. Driemeyer, "Ceramic matrix composite materials for engine exhaust systems on next-generation vertical lift vehicles," *J. Eng. Gas Turbines Power*, vol. 140, no. 10, Jun. 2018, doi: 10.1115/1.4040011.

[2] N. P. Bansal, *Handbook of Ceramic Composites*. Boston, USA: Kluwer Academic Publishers, 2005.

[3] L. Guo, G. Li, and Z. Gan, "Effects of surface roughness on CMAS corrosion behavior for thermal barrier coating applications," *J. Adv. Ceram.*, vol. 10, no. 3, pp. 472–481, Jun. 2021, doi: 10.1007/s40145-020-0449-7.

[4] J. L. Stokes, B. J. Harder, V. L. Wiesner, and D. E. Wolfe, "Melting and crystallization behavior of CaO-MgO-Al2O3-SiO2 silicates relevant to turbine engine applications," NASA/Langley Research Center, Hampton, VA, USA, 2021.

[5] E. Samayoa, "Resistance of ultra-high temperature ceramics to calcia-magnesia-alumina-silicate (CMAS) attack."

[6] J. L. Smialek, F. A. Archer, and R. G. Garlick, "Turbine airfoil degradation in the Persian Gulf War," *JOM*, vol. 46, no. 12, pp. 39–41, Dec. 1994, doi: 10.1007/BF03222663.

[7] C. G. Levi, J. W. Hutchinson, M.-H. Vidal-Sétif, and C. A. Johnson, "Environmental degradation of thermal-barrier coatings by molten deposits," *MRS Bull.*, vol. 37, no. 10, pp. 932–941, Oct. 2012, doi: 10.1557/mrs.2012.230.

[8] J. Engelbrecht, E. McDonald, J. Gillies, and A. Gertler, "Department of Defense Enhanced Particulate Matter Surveillance Program (EPMSP)," Desert Research Institute, Reno, NV, USA, Feb. 2008.

[9] J. R. Kelley, L. D. Wakeley, J. R. McKenna, and S. S. Jackson, "Physical characteristics of soil collected in Iraq and Afghanistan related to remote sensing," Defense Technical Information Center, Fort Belvoir, VA, Jan. 2010. doi: 10.21236/ADA592306.

[10] C. Ditzler, K. Scheffe, and Monger, H. C., *Soil Survey Manual*. in Agriculture Handbook, no. 18. Washington, D.C., USA: Government Printing Office, 2017.

[11] N. P. Opie, “A comparison of Afghanistan, Yuma, AZ, and manufactured sands melted on EB-PVD thermal barrier coatings.”

[12] D. J. de Wet, R. Taylor, and F. H. Stott, “Corrosion mechanisms of ZrO_2-Y_2O_3 thermal barrier coatings in the presence of molten middle-east sand,” *J. Phys. IV*, vol. 03, no. C9, pp. C9-655-C9-663, Dec. 1993, doi: 10.1051/jp4:1993969.

[13] N. P. Bansal and S. R. Choi, “Properties of desert sand and CMAS glass,” NASA, Glenn Research Center, Cleveland, OH, USA, 2014.

[14] V. L. Wiesner and N. P. Bansal, “Mechanical and thermal properties of calcium–magnesium aluminosilicate (CMAS) glass,” *J. Eur. Ceram. Soc.*, vol. 35, no. 10, pp. 2907–2914, Sep. 2015, doi: 10.1016/j.jeurceramsoc.2015.03.032.

[15] Z. Wu, Z. Wang, G. Shi, and J. Sheng, “Effect of surface oxidation on thermal shock resistance of the ZrB2–SiC–ZrC ceramic,” *Compos. Sci. Technol.*, vol. 71, no. 12, pp. 1501–1506, Aug. 2011, doi: 10.1016/j.compscitech.2011.06.008.

[16] S. Bose, *High Temperature Coatings*. Elsevier, Oxford, UK. 2007. doi: 10.1016/B978-0-7506-8252-7.X5000-8.

[17] N. P. Padture, M. Gell, and E. H. Jordan, “Thermal barrier coatings for gas-turbine engine applications,” *Science*, vol. 296, no. 5566, pp. 280–284, Apr. 2002, doi: 10.1126/science.1068609.

[18] A. Nieto, R. Agrawal, L. Bravo, C. Hofmeister-Mock, M. Pepi, and A. Ghoshal, “Calcia–magnesia–alumina–silicate (CMAS) attack mechanisms and roadmap towards Sandphobic thermal and environmental barrier coatings,” *Int. Mater. Rev.*, vol. 66, no. 7, pp. 451–492, Oct. 2021, doi: 10.1080/09506608.2020.1824414.

[19] W. G. Fahrenholtz, G. E. Hilmas, I. G. Talmy, and J. A. Zaykoski, “Refractory diborides of zirconium and hafnium,” *J. Am. Ceram. Soc.*, vol. 90, no. 5, pp. 1347–1364, May 2007, doi: 10.1111/j.1551-2916.2007.01583.x.

[20] F. G. Keihn and E. J. Keplin, “High-temperature thermal expansion of certain group IV and group V diborides,” *J. Am. Ceram. Soc.*, vol. 50, no. 2, pp. 81–84, Feb. 1967, doi: 10.1111/j.1151-2916.1967.tb15044.x.

[21] H. Wang *et al.*, “The fabrication and mechanical properties of SiC/ZrB2 laminated ceramic composite prepared by spark plasma sintering,” *Ceram. Int.*, vol. 38, no. 6, pp. 5015–5022, Aug. 2012, doi: 10.1016/j.ceramint.2012.02.098.

[22] W. Zhi, Q. Qiang, W. Zhanjun, and S. Guodong, "Effect of oxidation at 1100°C on the strength of ZrB2–SiC–graphite ceramics," *J. Alloys Compd.*, vol. 509, no. 24, pp. 6871–6875, Jun. 2011, doi: 10.1016/j.jallcom.2011.03.163.

[23] E. W. Neuman, "Elevated temperature mechanical properties of zirconium diboride based ceramics," Ph.D. dissertation, Materials Science and Engineering, Missouri S&T, Rolla, MO, USA, 2014.

[24] A. I. Bazhin, A. A. Goncharov, A. D. Pogrebnyak, V. A. Stupak, and S. A. Goncharova, "Superhardness effect in transition-metal diborides films," *Phys. Met. Metallogr.*, vol. 117, no. 6, pp. 594–601, Jun. 2016, doi: 10.1134/S0031918X16060028.

[25] M. Shahedi Asl, B. Nayebi, A. Motallebzadeh, and M. Shokouhimehr, "Nanoindentation and nanostructural characterization of ZrB2–SiC composite doped with graphite nano-flakes," *Compos. Part B Eng.*, vol. 175, p. 107153, Oct. 2019, doi: 10.1016/j.compositesb.2019.107153.

[26] E. J. Cheng *et al.*, "Mechanical properties of individual phases of ZrB2-ZrC eutectic composite measured by nanoindentation," *J. Eur. Ceram. Soc.*, vol. 37, no. 13, pp. 4223–4227, Oct. 2017, doi: 10.1016/j.jeurceramsoc.2017.05.031.

[27] V. Zamora, A. L. Ortiz, F. Guiberteau, and M. Nygren, "Spark-plasma sintering of ZrB2 ultra-high-temperature ceramics at lower temperature via nanoscale crystal refinement," *J. Eur. Ceram. Soc.*, vol. 32, no. 10, pp. 2529–2536, Aug. 2012, doi: 10.1016/j.jeurceramsoc.2012.02.023.

[28] H. J. Brown-Shaklee, W. G. Fahrenholtz, and G. E. Hilmas, "Densification behavior and thermal properties of hafnium diboride with the addition of boron carbides," *J. Am. Ceram. Soc.*, vol. 95, no. 6, pp. 2035–2043, Jun. 2012, doi: 10.1111/j.1551-2916.2012.05208.x.

[29] D.-W. Ni, J.-X. Liu, and G.-J. Zhang, "Pressureless sintering of HfB2–SiC ceramics doped with WC," *J. Eur. Ceram. Soc.*, vol. 32, no. 13, pp. 3627–3635, Oct. 2012, doi: 10.1016/j.jeurceramsoc.2012.05.001.

[30] C. Musa, R. Orrù, D. Sciti, L. Silvestroni, and G. Cao, "Synthesis, consolidation and characterization of monolithic and SiC whiskers reinforced HfB2 ceramics," *J. Eur. Ceram. Soc.*, vol. 33, no. 3, pp. 603–614, Mar. 2013, doi: 10.1016/j.jeurceramsoc.2012.10.004.

[31] E. Wuchina, E. Opila, M. Opeka, B. Fahrenholtz, and I. Talmy, "UHTCs: Ultra-high temperature ceramic materials for extreme environment applications," *Electrochem. Soc. Interface*, vol. 16, no. 4, pp. 30–36, Dec. 2007, doi: 10.1149/2.F04074IF.

[32] R. Tandon, H. Dumm, E. Corral, R. Loehman, and P. Kotula, "Ultra high temperature ceramics for hypersonic vehicle applications.," SAND2006-2925, 887260, Jan. 2006. doi: 10.2172/887260.

[33] A. Nieto, E. Samayoa, T. Ansell, and J. Luo, "Unusual temperature-dependent reactivity of ultra-high temperature ceramic (UHTC) borides with calcia-magnesia-alumina-silicate (CMAS)," *Materialia*, vol. 20, p. 101265, Dec. 2021, doi: 10.1016/j.mtla.2021.101265.

[34] K. Upadhya, P. Laboratory, E. Afb, and J. M. Yang, "Advanced materials for ultrahigh temperature structural applications above 2000 °C."

[35] C. B. Bargeron, R. C. Benson, R. W. Newman, A. N. Jette, and T. E. Phillips, "Oxidation mechanisms of hafnium carbide and hafnium diboride in the temperature range 1400 to 2100C."

[36] T. A. Parthasarathy, R. A. Rapp, M. Opeka, and R. J. Kerans, "A model for the oxidation of ZrB2, HfB2 and TiB2," *Acta Mater.*, vol. 55, no. 17, pp. 5999–6010, Oct. 2007, doi: 10.1016/j.actamat.2007.07.027.

[37] A. K. Kuriakose and J. L. Margrave, "The oxidation kinetics of zirconium diboride and zirconium carbide at high temperatures," *J. Electrochem. Soc.*, vol. 111, no. 7, p. 827, 1964, doi: 10.1149/1.2426263.

[38] J.-X. Liu, X.-Q. Shen, Y. Wu, F. Li, Y. Liang, and G.-J. Zhang, "Mechanical properties of hot-pressed high-entropy diboride-based ceramics," *J. Adv. Ceram.*, vol. 9, no. 4, pp. 503–510, Aug. 2020, doi: 10.1007/s40145-020-0383-8.

[39] Y. Zhang *et al.*, "Dense high-entropy boride ceramics with ultra-high hardness," *Scr. Mater.*, vol. 164, pp. 135–139, Apr. 2019, doi: 10.1016/j.scriptamat.2019.01.021.

[40] J. Gild *et al.*, "High-entropy metal diborides: A new class of high-etropy materials and a new type of ultrahigh temperature ceramics," *Sci. Rep.*, vol. 6, no. 1, p. 37946, Nov. 2016, doi: 10.1038/srep37946.

[41] M. Qin *et al.*, "Dual-phase high-entropy ultra-high temperature ceramics," *J. Eur. Ceram. Soc.*, vol. 40, no. 15, pp. 5037–5050, Dec. 2020, doi: 10.1016/j.jeurceramsoc.2020.05.040.

[42] L. Qiao *et al.*, "First-principles prediction, fabrication and characterization of (Hf0.2Nb0.2Ta0.2Ti0.2Zr0.2)B2 high-entropy borides," *Ceram. Int.*, vol. 48, no. 12, pp. 17234–17245, Jun. 2022, doi: 10.1016/j.ceramint.2022.02.281.

[43] H. Wang, S.-H. Lee, and H.-D. Kim, "Nano-hafnium diboride powders synthesized using a spark plasma sintering apparatus," *J. Am. Ceram. Soc.*, vol. 95, no. 5, pp. 1493–1496, May 2012, doi: 10.1111/j.1551-2916.2012.05141.x.

[44] G. B. Yadhukulakrishnan, S. Karumuri, A. Rahman, R. P. Singh, A. Kaan Kalkan, and S. P. Harimkar, "Spark plasma sintering of graphene reinforced zirconium diboride ultra-high temperature ceramic composites," *Ceram. Int.*, vol. 39, no. 6, pp. 6637–6646, Aug. 2013, doi: 10.1016/j.ceramint.2013.01.101.

[45] "AFRL 02 Test Dust," Powder Technology Inc. Arden Hills, MN, USA. https://www.powdertechnologyinc.com/product/afrl-02-test-dust/ (accessed Apr. 05, 2023).

[46] R. E. Chinn, "Grinding and polishing," in *Ceramography Preparation and Analysis of Ceramic Microstructures.*, Materials Park, OH, USA: ASM International, 2002, pp. 35–44.

THIS PAGE INTENTIONALLY LEFT BLANK

INITIAL DISTRIBUTION LIST

1. Defense Technical Information Center
   Ft. Belvoir, Virginia

2. Dudley Knox Library
   Naval Postgraduate School
   Monterey, California